Magnetism of complex metallic alloys: crystalline electric field effects

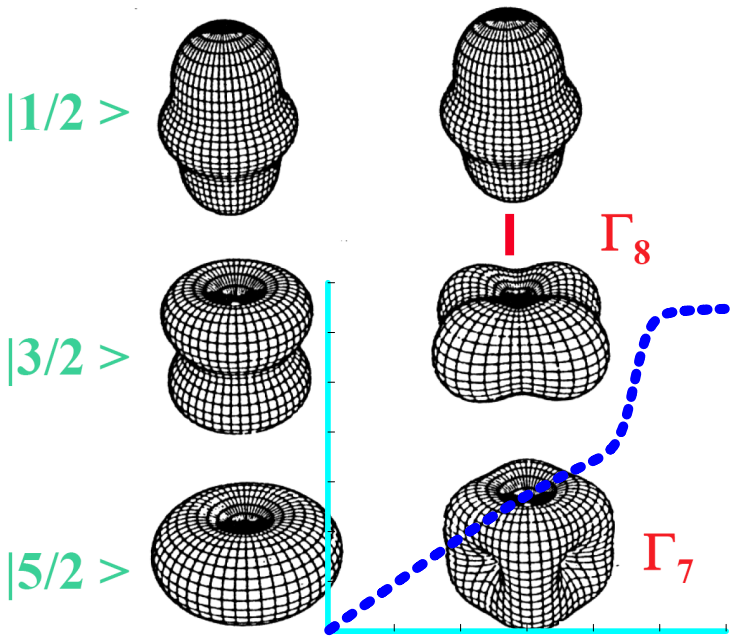

E. Bauer[1], M. Rotter [2]
[1]Institut für Festkörperphysik, Technische Universität Wien
[2]Institut für Physikalische Chemie, Universität Wien

A script for a lecture
given at the
CMA Euroschool 2007, Ljubljana, Slovenia
May 2007

Contents

1 Some aspects of the crystal field theory

In the following sections a brief overview on basic aspects of CEF theory is given and applications are mostly made in the context of Rare Earth ions which, in general, possess well defined localized magnetic moments as it is the case e.g., in filled skutterudites and in many other intermetallic compounds.

1.1 Magnetic properties of free ions

The Hamiltonian to describe magnetic atoms is given by

$$H_{tot} = H_0 + H_1 + H_{so} + H_{CF} + H_{Ze} \tag{1}$$

The various contributions are described in the following. The most important part is given by the sum of the kinetic energy and an effective radial potential.

$$H_0 = \sum_{i=1}^{N} \left(-\frac{\hbar^2}{2m}\Delta_i + V(r_i) \right) \tag{2}$$

Four quantum numbers n, l, m_l, m_s are satisfactory to describe the state of an electron in the atom (n ... principal quantum number, l ... orbital angular momentum quantum number, m_l, m_s are the respective magnetic quantum numbers).

- $l = 0, 1, 2, 3, \ldots, (n-1)$
- $m_l = -l, (-l+1), \ldots, 0, \ldots, (l-1), l$
- $s = 1/2$
- $m_s = \pm 1/2$

The eigenstates of the Hamiltonian H_0 are fully antisymmetric linear combinations of single electron wave functions, which are usually written down in the form of Slater determinants.

The most important perturbation to the radial symmetric Hamiltonian comes from the electrostatic electron-electron interaction and is represented by H_1.

$$H_1 = \frac{1}{8\pi\epsilon_0} \sum_{i \neq j} \frac{e^2}{r_{ij}} + \frac{1}{4\pi\epsilon_0} \sum_{i=1}^{N} \left(-\frac{Ze^2}{r_i} - V(r_i) \right) \tag{3}$$

In order to account for this interaction within a perturbation theory it is convenient to use linear combinations of Slater determinants, which are simultaneously eigenfunctions of H_0 and of the total orbital momentum operator $\boldsymbol{L}$ and of the total spin $\boldsymbol{S}$. The degeneracy of the ground state is partly lifted by considering the action of the electron-electron interaction H_1. The orbital and spin quantum numbers l and s of the ground state multiplet the follow from Hund's first and second rule [1].

- The combination of $\vec{s}_i$ that gives the lowest energy (i.e. the most stable) is that with the highest value of $(2s+1)$.
- If when the first rule has been satisfied there are several possible l values having the same value of $(2s+1)$, that with the largest l will be the most stable.

Hund's rules have full theoretical justification only in a very limited cases, but there are very little doubts of their validity. The argument to support them is as follows.

- Two electrons in the same orbital with opposite spins must involve large electrostatic electron-electron repulsion because of the proximity of the two electrons. Energy is lowered if dual occupations are minimised, giving as many like electrons as possible.
- Having satisfied the first condition, if the electrons orbit in the same sense electron-electron repulsive interactions are minimised because the electrons spend more of the time further apart.

Beside the kinetic- and the Coulomb energy, the spin-orbit coupling H_{so} and the crystal field interaction H_{CF} is of particular importance.

$$H_{so} = \sum_{i=1}^{N} \zeta(r_i) \vec{l}_i \vec{s}_i \tag{4}$$

$$H_{CF} = -|e| \sum_{i=1}^{N} V_c(\vec{r}_i) \tag{5}$$

Elements of the $3d$ and the $4f$ group possess permanent magnetic moments:

- 3d - series $\ldots l = 2$: Fe, Co, Cr, Mn $\ldots$;
- 4f - series $\ldots l = 3$: Ce, Nd, $\ldots$, Tm, Yb

While for $4f$ systems $H_{so} \gg H_{CF}$, $3d$ systems behave opposite: $H_{so} \ll H_{CF}$. The reason for this is (i) the fact that the $4f$ electron density is more concentrated in the inner part of the atom than that of the $3d$ electrons and consquently the crystal field experienced by the $4f$ electrons is screened by outer electrons. Furthermore (ii) the spin orbit interaction is proportional to the number of electrons and higher in the case of $4f$ electrons. Therefore to a good approximation the $3d$ elements can be treated in the strong coupling limit, i.e. $H_{so} \ll H_{CF}$. Usually the action of the crystal field leads to a ground state with $l = 0$ (quenching of the orbital moment). This can be understood by the simple argument, that the strong crystal field completely stops the orbital movement of the $3d$ electrons.

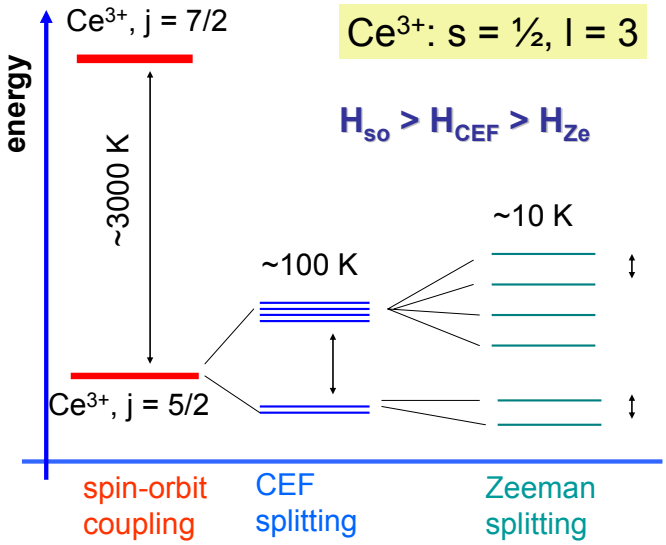

Figure 1: General splitting scheme of a 6-fold degenerate system.

In the following we will focus on the case of $4f$, where $H_{so} \gg H_{CF}$. [1] We now consider H_{so} as a perturbation to the ground state. It follows that m_l and m_s are no longer good quantum numbers because the spin orbit interaction does not commute with L_z and S_z. However, it commutes with $\boldsymbol{L}^2$ and $\boldsymbol{S}^2$ and all components of the total angular momentum $\boldsymbol{J} = \boldsymbol{L} + \boldsymbol{S}$. Therefore the multiplets of a free $4f$ ion can be characterized by the quantum numbers $|lsjm_j\rangle$. Fig. 1 gives an overview on the relevant energy scales of the problem.

The practical calculation of the total angular momentum follows then from Hund's third rule.

The most stable configurations result from

- $j = |l - s|$ ... less than half filled shells
- $j = |l + s|$ ... more than half filled shells
- $j = s$ ... half filled shell ($l = 0$).

The corresponding magnetic moments are

$$|\mu_L| = \mu_B |\boldsymbol{L}| = \mu_B \sqrt{l(l+1)}, \tag{6}$$

$$|\mu_s| = g_S \mu_B |\boldsymbol{S}| = 2\mu_B \sqrt{s(s+1)}, \tag{7}$$

[1] Note that for most rare earth elements this is a good approximation, exceptions are the Sm^{3+} and the Eu^{3+} ion with a spin orbit splitting of less than 100 meV.

where μ_B is the Bohr magneton. In a classsical view because of the spin-orbit interaction the resultant vectors $\vec{L}$ and $\vec{S}$ are precessing about their vector sum $\vec{J}$. To account for the different weight of the spin and the orbital contribution to the total angular momentum, the Landé factor g_j is introduced. In quantum mechanical terms the Landé factor is introduced by applying the Wigner Eckhardt theorem to the ground state matrix elements of the total magnetic moment, which is given by:

$$\vec{\mu} = \vec{\mu}_L + \vec{\mu}_S = \mu_B(\boldsymbol{L} + 2\boldsymbol{S}) \tag{8}$$

According to the Wigner Eckhardt theorem within the ground state multiplet $|lsj, m_j = -j, \ldots, +j >$ the matrix elements of any pair of vectors (such as for instance the magnetic spin moment and the total angular momentum) are proportional. Applying this relation to the total magnetic moment and the total angular moment yields

$$|\mu| = g_j \mu_B \sqrt{j(j+1)} \tag{9}$$

with the Landé factor

$$g_j = 1 + \frac{j(j+1) + s(s+1) - l(l+1)}{2j(j+1)} \tag{10}$$

Borderline cases: $g_j = 2$ for $l = 0$ and $g_j = 1$ for $s = 0$. This defines the magnetic moment of a single atom. Assuming for the moment, that the crystal field interaction is zero, the magnetic properties of free ions can be discussed.

In the absence of external magnetic fields, all the atoms with equal magnetic moments have equal energy. If an external magnetic field $\vec{B}$ is applied, this degeneracy is lifted by the action of H_{Ze}.

$$H_{Ze} = -\vec{\mu}\vec{B} \tag{11}$$

Provided that the field is applied along the z-axis, the different eigenstates can be characterized by the magnetic quantum number m_j, the corresponding energies are

$$E_{m_j} = -\langle lsjm_j|\vec{\mu}|lsjm_j\rangle \cdot \vec{B} = -g\mu_B m_j B \tag{12}$$

Then the energy depends on the thermal occupation of the $2j + 1$ sub-levels, all of which differ in their m_j value.

The magnetic sub-levels are occupied according to the laws of statistical mechanics, the lowest energy having the largest population. The relative population P of a sublevel m_j is given by

$$P(m_j) = \frac{\exp(-E_{m_j}/k_B T)}{\sum \exp(-E_{m_j}/k_B T)}. \tag{13}$$

1.2 CEF Hamiltonian

Similar to a magnetic field, an electric field is able to lift, at least partially, the $(2j+1)$-fold degenerate ground state. Such an electric field may be created by the ions surrounding regularly a rare earth ion in a crystal. According to the Kramers theorem, there remains a certain degeneracy of the states:

- if the total angular momentum is half-integer, i.e, $j = 5/2, 7/2, 9/2\ldots$, the minimum degeneracy is 2; such a state is a *doublet*. These systems are so called *Kramers ions*.
- if the total angular momentum is integer, i.e, $j = 4, 5, 6\ldots$, the degeneracy can be totally lifted. But in general, there is a mixture of singlet, doublet, triplet and quartet states. These systems are so called *non-Kramers ions*.

The particular scheme of a system is determined from material dependent properties such as charges, but independently depends on both the total angular momentum and the crystal symmetry. A lower symmetry causes lower degeneracies of levels. Quartets may be found in cubic structures only.

Assume that a $4f$-ion is situated in a potential V_c, which is created from the neighbouring ions (compare Fig. 2). This potential acts in a similar way as the *Stark-effect*

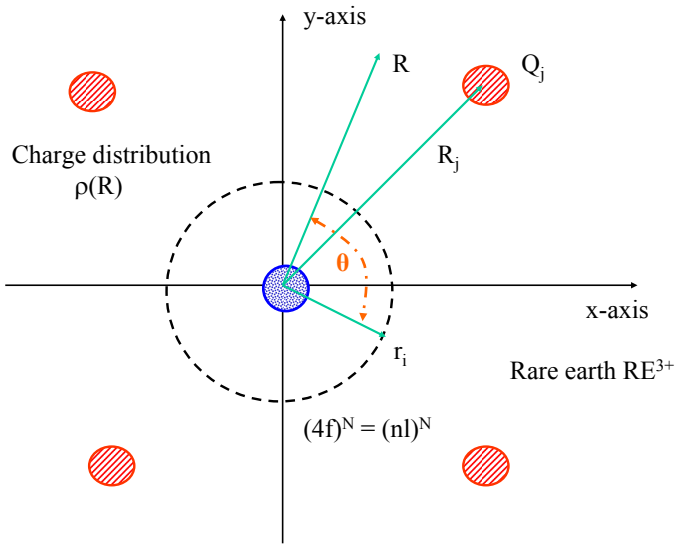

Figure 2: Geometric relations for the determination of the crystal electric field.

and causes, at least, a partial lifting of the $(2j+1)$-fold ground state degeneracy of the free $4f$ ion. If we further assume that the $4f$ wavefunctions do not overlap with that of the neighbouring ions, then the potential $V_c(\vec{r})$ fulfils Laplace's equation, i.e.,

$\nabla^2 V_c = 0$ and for the crystal field contribution the following relation is valid:

$$V_c(\vec{r}) = \frac{1}{4\pi\epsilon_0} \int \frac{\rho(\vec{R})}{|\vec{r} - \vec{R}|} d^3R \tag{14}$$

with a charge density $\rho(\vec{R})$ and the series expansion

$$\frac{1}{|\vec{r} - \vec{R}|} = \frac{1}{\sqrt{(r^2 + R^2 - 2rR\cos\theta)}} = \frac{1}{R} \sum_{l=0}^{\infty} \left(\frac{r}{R}\right)^l P_l(\cos\theta) \tag{15}$$

for all $r < R$. The Legendre-polynoms $P_l(\cos\theta)$ can be expressed in terms of spherical harmonics $Y_l^m \ldots$.

$$P_l(\cos\theta) = \frac{4\pi}{2l+1} \sum_{m=-l}^{l} Y_l^m(\Omega_r) Y_l^{m*}(\Omega_R). \tag{16}$$

If it is assumed that the ions $i = 1, 2, 3, ...$ carry point charges q_i (*point charge model, PCM*) we have

$$V_c(\vec{r}) = \frac{1}{4\pi\epsilon_0} \sum_i \frac{q_i}{|\vec{r} - \vec{R}_i|} \tag{17}$$

In the following we will not use the expansion (16) but instead of spherical harmonics use tesseral harmonics, which are real and defined according to [2][2] and listed explicitely in appendix B.

$$\begin{aligned} Z_l^0 &= Y_l^0 \\ Z_l^m &= \frac{1}{\sqrt{2}} \left[Y_l^{-m} + (-1)^m Y_l^m\right] \ldots m > 0 \\ Z_l^m &= \frac{i}{\sqrt{2}} \left[Y_l^m + (-1)^m Y_l^{-m}\right] \ldots m < 0 \end{aligned} \tag{18}$$

Inserting the tesseral harmonics into Eqn. (16) leads to

$$V_c(\vec{r}) = \sum_{l=0}^{\infty} \sum_{m=-l}^{l} r^l Z_l^m(\Omega_r) \frac{1}{2l+1} \int d^3R \frac{\rho(\vec{R}) Z_l^m(\Omega_R)}{\epsilon_0 R^{l+1}} \tag{19}$$

If on the r.h.s. of this equation the following substitutions [3, 4]

$$\gamma_l^m = \frac{1}{2l+1} \int d^3R \frac{\rho(\vec{R}) Z_l^m(\Omega_R)}{\epsilon_0 R^{l+1}} \tag{20}$$

[2]note that there are different definitions of tesseral harmonic functions in the literature, we use here the definition given in [2]

and

$$H_{lm} = \sum_{i=1}^{N} r_i^l Z_l^m(\delta_i, \phi_i) \tag{21}$$

are made, the crystal field Hamiltonian can be expressed as

$$H_{CF} = -|e| \sum_{i=1}^{N} V_c(\vec{r}_i) = \sum_{l,m} \gamma_l^m H_{lm}. \tag{22}$$

For a given multiplet, the matrix elements of H_{CF} are proportional to those of *equivalent operators*, which contain J_z or $J_\pm$ (*Wigner-Eckhart-theorem*).

Example:

$$H_2^0 = \sum_i r_i^2 \sqrt{\frac{5}{4\pi}} \frac{1}{2} \left(3\cos^2\delta_i - 1\right) = \sum_i r_i^2 \sqrt{\frac{5}{4\pi}} \frac{1}{2} \left(\frac{3z_i^2 - r_i^2}{r_i^2}\right) \tag{23}$$

Here we have made the following assignments (spherical-polar co-ordinates):

$$x = r\sin\delta\cos\phi \rightarrow J_x$$

$$y = r\sin\delta\sin\phi \rightarrow J_y$$

$$z = r\cos\delta \rightarrow J_z \qquad r \rightarrow J$$

as well as

$$xy \rightarrow (1/2)(J_x J_y + J_y J_x)$$

and

$$J_\pm = J_x \pm i J_y$$

For example, the matrix elements of the crystal field Hamiltonian H_2^0 within the ground state multiplett $|lsjm_j\rangle$ of a rare earth ion can be written as

$$\begin{aligned} \langle lsjm_j|H_2^0|lsjm_j'\rangle &= \langle lsjm_j| \sum_i r_i^2 \sqrt{\frac{5}{4\pi}} \frac{1}{2} \left(\frac{3z_i^2 - r_i^2}{r_i^2}\right) |lsjm_j'\rangle \\ &= \sqrt{\frac{5}{4\pi}} \frac{1}{2} \alpha_J \langle r^2\rangle \langle lsjm_j| \left(3J_z^2 - j(j+1)\right) |lsjm_j'\rangle \end{aligned} \tag{24}$$

with the radial matrix elements defined by

$$\langle r^l\rangle = \int |R_{4f}(r)|^2 r^{l+2} dr \tag{25}$$

These matrix elements have been calculated for different rare earth atoms using the $4f$ radial wave functions $R_{4f}(r)$ as determined by the Hartree Fock method or similar, see e.g. [5, 6].

By defining Stevens operators O_l^m according to a few rules [7], e.g.,

$$O_2^0 = \left(3J_z^2 - j(j+1)\right) \tag{26}$$

Table 1: Orbital (l), spin (s) and total angular momentum (j) quantum numbers, Landé factor g_j and Stevens factors $\alpha_j, \beta_j, \gamma_j$ for rare earth and actinide ions.

ion	l	s	j	g_j	$\alpha_j \times 10^2$	$\beta_j \times 10^4$	$\gamma_j \times 10^6$
Ce^{3+}	3	1/2	5/2	6/7	-5.7143	63.4921	0.0000
Pr^{3+},Ce^{2+},U^{4+}	5	1	4	4/5	-2.1010	-7.3462	60.9940
Nd^{3+},Pr^{2+},U^{3+},Np^{4+}	6	3/2	9/2	8/11	-0.6428	-2.9111	-37.9880
Pm^{3+},Nd^{2+}	6	2	4	3/5	0.7713	4.0755	60.7807
Sm^{3+},Pm^{2+}	5	5/2	5/2	2/7	4.1270	25.0120	0.0000
Eu^{3+},Sm^{2+}	3	3	0	-	0.0000	0.0000	0.0000
Gd^{3+},Eu^{2+}	0	7/2	7/2	2	0.0000	0.0000	0.0000
Tb^{3+},Gd^{2+}	3	3	6	3/2	-1.0101	1.2244	-1.1212
Dy^{3+},Tb^{2+}	5	5/2	15/2	4/3	-0.6349	-0.5920	1.0350
Ho^{3+},Dy^{2+}	6	2	8	5/4	-0.2222	-0.3330	-1.2937
Er^{3+},Ho^{2+}	6	3/2	15/2	6/5	0.2540	0.4440	2.0699
Tm^{3+},Er^{2+}	5	1	6	7/6	1.0101	1.6325	-5.6061
Yb^{3+},Tm^{2+}	3	1/2	7/2	8/7	3.1746	-17.3160	148.0001

the operators which initially were spatial dependent are now simply proportional to angular momentum operators. For each tesseral harmonic function a Stevens operator can be defined by substituting x, y and z by the components J_x, J_y and J_z, respectively and symmetrizing the resulting expression. A complete list of these Stevens operators is given in appendix A. In addition, the coefficients of the polynoms in x,y and z in the definition of the tesseral functions are denoted by p_l^m, e.g.

$$p_2^0 = \sqrt{\frac{5}{4\pi}}\frac{1}{2} \tag{27}$$

Dropping for simplicity the $\langle lsjm_j|$ in the notation and keeping in mind, that the following equations hold only for the matrix elements of the ground state multiplet of the rare earth ion this yields

$$\begin{aligned} H_2^0 &= \sum_i r_i^2 \sqrt{\frac{5}{4\pi}}\frac{1}{2}\left(\frac{3z_i^2 - r_i^2}{r_i^2}\right) && (28) \\ &\rightarrow p_2^0 \alpha_j \langle r^2 \rangle O_2^0(\vec{J}) && (29) \end{aligned}$$

and in general

$$H_l^m = \sum_i r_i^l Z_l^m(\Omega_i) = p_l^m \Theta_l \langle r^l \rangle O_l^m(\vec{J}) \tag{30}$$

Table 2: List of radial matrix elements $\langle r^l \rangle$ for l = 2, 4 and 6 for rare earth and actinide ions [6, 8, 4]

ion	$\langle r^2 \rangle$(Å^2)	$\langle r^4 \rangle$(Å^4)	$\langle r^6 \rangle$(Å^6)
Ce^{3+}	0.3666	0.3108	0.5119
Pr^{3+}	0.3350	0.2614	0.4030
Nd^{3+}	0.3120	0.2282	0.3300
Pm^{3+}	0.2899	0.1991	0.2755
Sm^{3+}	0.2728	0.1772	0.2317
Eu^{3+}	0.2569	0.1584	0.1985
Gd^{3+}	0.2428	0.1427	0.1720
Tb^{3+}	0.2302	0.1295	0.1505
Dy^{3+}	0.2188	0.1180	0.1328
Ho^{3+}	0.2085	0.1081	0.1181
Er^{3+}	0.1991	0.0996	0.1058
Tm^{3+}	0.1905	0.0921	0.0953
Yb^{3+}	0.1826	0.0854	0.0863
U^{4+}	0.5718	0.5985	1.0491
U^{3+}	0.6569	0.8552	1.9882
Np^{4+}	0.5276	0.5100	0.8300
Nd^{2+}	0.3898	0.4191	0.9980
Sm^{2+}	0.3352	0.3028	0.6271
Eu^{2+}	0.3075	0.2641	0.5178
Gd^{2+}	0.2879	0.2333	0.4359
Tb^{2+}	0.2711	0.2082	0.3729
Dy^{2+}	0.2557	0.1875	0.3235
Ho^{2+}	0.2425	0.1701	0.2837
Er^{2+}	0.2307	0.1552	0.2514
Tm^{2+}	0.2198	0.1426	0.2249
Yb^{2+}	0.2100	0.1315	0.2027

This leads to the famous notation

$$H_{CF} = \sum_{l,m} B_l^m O_l^m \tag{31}$$

with

$$B_l^m = -|e| p_l^m \gamma_l^m \langle r_{4f}^l \rangle \Theta_l \tag{32}$$

$$\Theta_l = \begin{cases} \alpha_j & \dots \quad l = 2 \\ \beta_j & \dots \quad l = 4 \\ \gamma_j & \dots \quad l = 6 \end{cases} \tag{33}$$

The B_l^m or γ_l^m are the crystal field parameters, which can be determined from the experiment, or can be calculated from different models among them the PCM. The additional parameters and coefficients are already tabulated and given in tables 1 and 2.

1.3 Symmetry considerations

1.3.1 Disappearance of terms with $l \neq 2, 4, 6$

A major simplification of the theory is due to the fact that for $4f$ electrons all terms with $l > 6$ disappear in equation (31). This is due to the fact that the $4f$ wave functions $\langle lsjm_j|$ are a linear combination of Slater Determinants of single particle wave functions of the form $\Phi_{4f}^{mm_s}(\vec{r}) = R_{4f}(r) Y_3^m(\Omega) \chi_i^{m_s}$. Therefore, the matrix elements of $r^l Z_l^m(\Omega)$ in (30) are a linear combination of integrals of the form

$$\int \Phi_{4f}^{mm_s *}(\vec{r}) r^l Y_l^{m''}(\Omega) \Phi_{4f}^{m'm'_s}(\vec{r}) r^2 dr d\Omega = \langle r^l \rangle \delta_{m_s m'_s} \int (-1)^m Y_3^{-m}(\Omega) Y_l^{m''}(\Omega) Y_3^{m'}(\Omega) d\Omega \tag{34}$$

From elementary quantum mechanics it is known, that the spherical harmonics Y_l^m are eigenfunctions of the angular momentum operator. The addition of angular momentum is done according to the Clebsch Gordon expansion. From this Clebsch Gordan expansion the spherical harmonic addition relation can be derived (for a proof see for example [9], page 1046, Eqn. 21), which for the special case of $l = 3$ can be written as

$$Y_3^{-m}(\Omega) Y_3^{m'}(\Omega) = \sum_{l=0}^{6} \sum_{m''=-l}^{l} \frac{7}{\sqrt{4\pi(2l+1)}} \langle 3,3;0,0|l,0\rangle \langle 3,3;-m,m'|l,m'' > Y_l^{m''}(\Omega) \tag{35}$$

The product in Eqn. (34) can be written as a linear combination of products of two spherical harmonics, where l takes the values $l = 0, \dots, 6$. Moreover, keeping in mind that the Clebsch-Gordon coefficients fulfil the symmetry relation

$\langle l_1, l_2; -m_1, -m_2 | l, m\rangle = (-1)^{l_1+l_2+l}\langle l_1, l_2; m_1, m_2 | l, m\rangle$ we note that the coefficient $\langle 3, 3; 0, 0 | l, 0\rangle$ is zero for odd l. Because of the orthogonality of the spherical harmonics all terms with $l \neq 2, 4, 6$ disappear in Eq. (34) and consequently also in (31).

1.3.2 Disappearance of CEF parameters due to Point Symmetry of the CEF

If coordinate axes are properly chosen the local point symmetry at the rare earth site further limits the number of nonzero crystal field parameters. In order to discuss this issue we refer to the definition of the coefficients γ_l^m in Eqn. (20).

the z-axis is an p-fold axis of symmetry keeping in mind that the tesseral harmonics are a sum of spherical harmonics and the the ϕ dependence of these is given by $e^{im\phi}$ such a symmetry axis allows to split the integral in (20) into a sum of p integrals. These only differ by the factor $e^{im2\pi/p}$. Consequently, the coefficients γ_l^m are proportional to the sum $\sum_{s=0}^{p-1} e^{im2\pi s/p}$, which is a geometrical sum $\sum_{s=0}^{p-1} x^s = (1-x^p)/(1-x)$). Accordingly, *the γ_l^m vanish unless m is a integer multiple of p .*

the y-axis is a twofold axis of symmetry such a twofold symmetry axis is described in polar coordinates by the tranformation $\Theta \to \pi - \Theta$ and $\phi \to -\pi - \phi$. Writing the integral in (20) as a sum of two integrals and applying this transformation and using the relations $Y_l^m(\Theta, -\phi) = (-1)^m Y_l^m(\Theta, \phi)$, $Y_l^m(\Theta - \pi, \phi + \pi) = (-1)^l Y_l^m(\Theta, \phi)$ leads to a factor $1 + (-1)^{l+m}$. Consequently, all γ_l^m *with $l + m$ odd vanish.*

Such Symmetry considerations allowed to compile table 3, where the nonvanishing crystal field parameters for all crystallographic point groups are given.

Table 3: Possible local symmetries and corresponding non zero CEF parameters. In the case when $m > 0$ and both parameters B_l^m and B_l^{-m} are nonzero, one of these B_l^m with $m > 0$ can by made zero by a rotation of the coordinate system. However, the appropriate orientation of the coordinate system in these cases a priori. It requires the knowledge of the crystal field parameters. Note, that for cubic symmetry additionally $B_4^4 = \frac{5}{2} B_4^0$ and $B_6^4 = -\frac{21}{2} B_6^0$. For the icosahedral case (not compatible with translational symmetry) B_6^5=-42B_6^0 [10].

symmetry		B_2^0	$B_2^{\pm1}$	$B_2^{\pm2}$	B_4^0	$B_4^{\pm1}$	$B_4^{\pm2}$	$B_4^{\pm3}$	$B_4^{\pm4}$	B_6^0	$B_6^{\pm1}$	$B_6^{\pm2}$	$B_6^{\pm3}$	$B_6^{\pm4}$	$B_6^{\pm5}$	$B_6^{\pm6}$
triclinic	C_i C_1	+	±	±	+	±	±	±	±	+	±	±	±	±	±	±
monoclinic	C_2 C_s C_{2h}	+		±	+		±		±	+		±		±		±
rhombic	C_{2v} D_2 D_{2h}	+		+	+		+		+	+		+		+		+
tetragonal	C_4 S_4 C_{4h}	+			+				±	+				±		
tetragonal	D_4 C_{4v} D_{2d} D_{4h}	+			+				+	+				+		
trigonal	C_3 S_6	+			+			±		+			±			±
trigonal	D_3 C_{3v} D_{3d}	+			+			+		+			+			+
hexagonal	C_6 C_{3h} C_{6h}	+			+					+						±
hexagonal	D_6 C_{6v} D_{3h} D_{6h}	+			+					+						+
cubic	T T_d T_h O O_h				+				+	+				+		
icosahedral	I_h									+					+	

1.4 Cubic and hexagonal symmetries

If the crystal field Hamiltonian is applied onto the wave function of the $4f$ ion, one obtains the energies of the eigenstates created by crystal field splitting.

$$H_{CF}|\Psi\rangle = E|\Psi\rangle \tag{36}$$

In the case of a cubic point group symmetry, the appropriate crystal field Hamiltonian is given by

$$H_{CF}^{cub.} = B_4^0\left(O_4^0 + 5O_4^4\right) + B_6^0\left(O_6^0 - 21O_6^6\right) \tag{37}$$

The crystal field is fully determined by 2 parameters B_4^0 and B_6^0. For Ce^{3+} we have additionally $\gamma_j = 0$; i.e., in this case B_4^0 is the *only* relevant parameter.

The resulting eigenstates are a Γ_7-doublet and a Γ_8-quartet

$$\begin{aligned} |\Gamma_7\rangle &= a|\pm 5/2\rangle - b|\mp 3/2\rangle \\ |\Gamma_8\rangle &= \begin{cases} |\pm 1/2\rangle \\ b|\pm 5/2\rangle + a|\mp 3/2\rangle \end{cases} \end{aligned} \tag{38}$$

which can be represented in terms of J_z with $a = (1/6)^{1/2}$ and $b = (5/6)^{1/2}$. For a Ce^{3+} ion it follows immediately

$$B_4^0 = \pm\Delta/360 \tag{39}$$

There, Δ is the energy difference between Γ_7 and Γ_8. In Fig. 3 is displayed the $4f$ charge density of a cerium 3+ ion for a cubic symmetry.

The crystal field Hamiltonian for hexagonal symmetry is written as

$$H_{CF}^{hexa} = B_2^0 O_2^0 + B_4^0 0_4^0 + B_6^0 O_6^0 + B_6^6 O_6^6 \tag{40}$$

Again, 6-th order term vanishes in the case of cerium systems; therefore,

$${}^{\mathrm{Ce}}H_{CF}^{hexa} = B_2^0 O_2^0 + B_4^0 0_4^0 \tag{41}$$

The crystal field in hexagonal symmetry yields "pure" eigenstates, determined from J_z. If we assume that

$$|\Gamma_7\rangle = |\pm 1/2\rangle \tag{42}$$

$$|\Gamma_8\rangle = |\pm 5/2\rangle \tag{43}$$

$$|\Gamma_9\rangle = |\pm 3/2\rangle \tag{44}$$

the energies of a crystal field doublet are calculated owing to the application of

$$H_{CF}|\Psi_\Gamma\rangle = E_\Gamma|\Psi_\Gamma\rangle \tag{45}$$

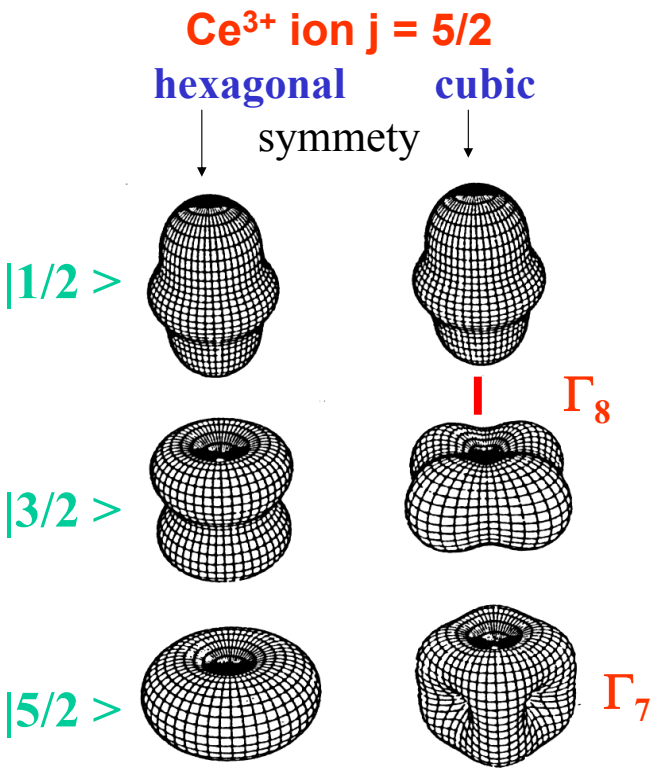

Figure 3: Contours of the $4f$ charge density of a Ce^{3+} ion in hexagonal (a) and in cubic (b) symmetry.

i.e.,

$$E_7 = -8B_2^0 + 120B_4^0 \quad (46)$$
$$E_8 = 10B_2^0 + 60B_4^0 \quad (47)$$
$$E_9 = -2B_2^0 - 180B_4^0. \quad (48)$$

The charge density distribution of a Ce^{3+} ion created from the crystal electric field is also shown in Fig. 3.

1.5 Example: an Yb ion in a hexagonal crystalline electric field

Recall that the crystal field Hamiltonian for hexagonal systems reads (see table 3 and Eqn. 40):

$$H_{CF}^{hexa} = B_2^0 O_2^0 + B_4^0 O_4^0 + B_6^0 O_6^0 + B_6^6 O_6^6 \quad (49)$$

where the Stevens operators are given by (see the appendix):

$$O_2^0 = [3J_z^2 - X] \quad \text{with} \quad X = j(j+1)$$

$$O_4^0 = [35J_z^4 - (30X - 25)J_z^2 + 3X^2 - 6X]$$

$$O_6^0 = [231J_z^6 - (315X - 735)J_z^4 + (105X^2 - 525X + 294)J_z^2 - 5X^3 + 40X^2 - 60X]$$

$$O_6^6 = \frac{1}{2}[J_+^6 + J_-^6].$$

In the subsequent section we outline in a step-by-step path all details to evaluate the eigenvalues and the eigenstates of the CEF levels of a typical compound based on the rare earth element Yb, crystallizing in a hexagonal crystal structure. Moreover, we assume that the electronic environment can be composed from a number of point charges. Yb should be in its trivalent state, i.e, Yb^{3+}. This state can be associated with electronic configuration $4f^{13}$ revealing a total angular momentum $j = 7/2$ and an effective magnetic moment $\mu_{eff} = 4.54\ \mu_B$.

Writing for simplicity m instead of m_j, the following notations and rules apply for practical calculations:

$$J_+ \equiv J_x + \mathrm{i}J_y \qquad J_- \equiv J_x - \mathrm{i}J_y$$

$$J_+|jm\rangle = [j(j+1) - m(m+1)]^{1/2}|jm+1\rangle$$
$$J_-|jm\rangle = [j(j+1) - m(m-1)]^{1/2}|jm-1\rangle$$
$$J_z|jm\rangle = m|jm\rangle$$
$$\boldsymbol{J}^2|jm\rangle = j(j+1)|jm\rangle$$
$$\langle jm|j'm'\rangle = \delta_{mm'}\delta_{jj'}$$

The individual contributions of the various O_l^m will now be evaluated by computing the respective matrix elements.

1.5.1 The Crystal Field Hamiltonian in Matrix Notation

$\mathbf{O_2^0}$: All those states will be combined and displayed, which reveal finite matrix elements for O_2^0.

$$O_2^0 = 3J_z^2 - j(j+1)$$

$$3[\langle -7/2|J_z^2|-7/2\rangle] - 7/2(7/2+1) = 21$$

$$3[\langle -5/2|J_z^2|5/2\rangle - 7/2(7/2+1) = 3$$

$$3[\langle -3/2|J_z^2|-3/2\rangle - 7/2(7/2+1) = -9$$

$$3[\langle -1/2|J_z^2|-1/2\rangle - 7/2(7/2+1) = -15$$

$$3[\langle 1/2|J_z^2|1/2\rangle - 7/2(7/2+1) = -15$$

$$3[\langle 3/2|J_z^2|3/2\rangle - 7/2(7/2+1) = -9$$

$$3[\langle 5/2|J_z^2|5/2\rangle - 7/2(7/2+1) = 3$$

$$3[\langle 7/2|J_z^2|7/2\rangle - 7/2(7/2+1) = -9$$

$\mathbf{O_4^0}$

$$O_4^0 = [35J_z^4 - 30\boldsymbol{J}^2 J_z^2 + 25J_z^2 - 6\boldsymbol{J}^2 + 3\boldsymbol{J}^4]$$

$$35[\langle -7/2|J_z^4|-7/2\rangle] - 30\cdot(7/2)\cdot(9/2)[\langle -7/2|J_z^2|-7/2\rangle] +$$

$$25[\langle -7/2|J_z^2|-7/2\rangle] - 6\cdot(7/2)\cdot(9/2) + 3\cdot(7/2)^2\cdot(9/2)^2 = 420$$

$$35[\langle -5/2|J_z^4|-5/2\rangle] - 30\boldsymbol{J}^2[\langle -5/2|J_z^2|-5/2\rangle] +$$

$$25[\langle -5/2|J_z^2|-5/2\rangle] - 6\cdot(7/2)\cdot(9/2) + 3\cdot(7/2)^2\cdot(9/2)^2 = -780$$

$$\langle -3/2|\ldots|-3/2\rangle = -180$$

$$\langle -1/2|\ldots|-1/2\rangle = 540$$

The matrix elements associated with +1/2, +3/2, +5/2, +7/2 have the same values as the above one with -1/2, -3/2, -5/2, -7/2.

$\mathbf{O_6^0}$

$$231[\langle -7/2|J_z^6|-7/2\rangle] - 315\cdot(7/2)\cdot(9/2)[\langle -7/2|J_z^4|-7/2\rangle] +$$

$$735[\langle -7/2|J_z^4|-7/2\rangle] + 105\cdot(7/2)^2\cdot(9/2)^2[\langle -7/2|J_z^2|-7/2\rangle] -$$

$$525\cdot(7/2)\cdot(9/2)[\langle -7/2|J_z^2|-7/2\rangle] + 294[\langle -7/2|J_z^2|-7/2\rangle] -$$

$$5\cdot(7/2)^3\cdot(9/2)^3 + 40\cdot(7/2)^2\cdot(9/2)^2 + 60\cdot(7/2)\cdot(9/2) = 1260$$

$$\langle -5/2|\ldots|-5/2\rangle = -6300$$

$$\langle -3/2|\ldots|-3/2\rangle = 11340$$

$$\langle -1/2|\ldots|-1/2\rangle = -6300$$

$\mathbf{O_6^6}$: The subsequent equations demonstrate how the ladder operators exert on a certain state.

$$J_+^6|-7/2\rangle \propto c_5 J_+^5|-5/2\rangle \propto c_4 J_+^4|-3/2\rangle \propto c_3 J_+^3|-1/2\rangle \propto c_2 J_+^2|+1/2\rangle \propto c_1 J_+|3/2\rangle = c|5/2\rangle$$

$$J_+^6|-5/2\rangle \propto d_5 J_+^5|-3/2\rangle \propto d_4 J_+^4|-1/2\rangle \propto d_3 J_+^3|1/2\rangle \propto d_2 J_+^2|+3/2\rangle \propto d_1 J_+|5/2\rangle = d|7/2\rangle$$

$$J_-^6|7/2\rangle \ldots = f|-5/2\rangle$$

$$J_-^6|5/2\rangle \ldots = g|-7/2\rangle.$$

Let us now evaluate in detail $J_+^6|j,m\rangle = J_+^6|7/2,-7/2\rangle$:

$$[j(j+1)-m(m+1)]^{1/2} = [(7/2)\cdot(9/2)-(-7/2)\cdot(-5/2)]^{1/2} = [(63/4)-(35/4)]^{1/2} = \sqrt{7}$$

and

$$J_+^6|7/2,-7/2\rangle = \sqrt{7}J_+^5|7/2,-5/2\rangle = \sqrt{7}[(63/4)-(15/4)]^{1/2}J_+^4|7/2,-3/2\rangle =$$

$$\sqrt{7\cdot 12}[(63/4)-(3/4)]^{1/2}J_+^3|7/2,-1/2\rangle = \sqrt{7\cdot 12\cdot 15}[(63/4)-(1/2)(1/2)]^{1/2}J_+^2|7/2,1/2\rangle =$$

$$\sqrt{7\cdot 12\cdot 15\cdot 16}[(63/4)-(1/2)(3/2)]^{1/2}J_+|7/2,3/2\rangle =$$

$$\sqrt{7\cdot 12\cdot 15\cdot 16\cdot 15}[(63/4)-(3/2)(5/2)]^{1/2}|7/2,5/2\rangle =$$

$$\sqrt{7\cdot 12\cdot 15\cdot 16\cdot 15\cdot 12}|7/2,5/2\rangle = 720\sqrt{7}|7/2,5/2\rangle$$

It follows that

$$\langle 5/2|J_+^6|-7/2\rangle = 720\sqrt{7}$$

$$\langle 7/2|J_+^6|-5/2\rangle = 720\sqrt{7}$$

$$\langle -7/2|J_-^6|5/2\rangle = 720\sqrt{7}$$

$$\langle -5/2|J_-^6|7/2\rangle = 720\sqrt{7}$$

Adding together all terms to form 8×8 matrices reveals for the hexagonal case

$$
{}^{7/2}H_{CF}^{hexa} = B_2^0 \times \begin{array}{c} \\ \mathbf{-7/2} \\ \mathbf{-5/2} \\ \mathbf{-3/2} \\ \mathbf{-1/2} \\ \mathbf{1/2} \\ \mathbf{3/2} \\ \mathbf{5/2} \\ \mathbf{7/2} \end{array} \begin{array}{c} \begin{array}{cccccccc} \mathbf{-7/2} & \mathbf{-5/2} & \mathbf{-3/2} & \mathbf{-1/2} & \mathbf{1/2} & \mathbf{3/2} & \mathbf{5/2} & \mathbf{7/2} \end{array} \\ \begin{pmatrix} 21 & 0 & 0 & 0 & 0 & 0 & 0 & 0 \\ 0 & 3 & 0 & 0 & 0 & 0 & 0 & 0 \\ 0 & 0 & -9 & 0 & 0 & 0 & 0 & 0 \\ 0 & 0 & 0 & -15 & 0 & 0 & 0 & 0 \\ 0 & 0 & 0 & 0 & -15 & 0 & 0 & 0 \\ 0 & 0 & 0 & 0 & 0 & -9 & 0 & 0 \\ 0 & 0 & 0 & 0 & 0 & 0 & 3 & 0 \\ 0 & 0 & 0 & 0 & 0 & 0 & 0 & 21 \end{pmatrix} \end{array} +
$$

$$
+ B_4^0 \times \begin{array}{c} \\ \mathbf{-7/2} \\ \mathbf{-5/2} \\ \mathbf{-3/2} \\ \mathbf{-1/2} \\ \mathbf{1/2} \\ \mathbf{3/2} \\ \mathbf{5/2} \\ \mathbf{7/2} \end{array} \begin{array}{c} \begin{array}{cccccccc} \mathbf{-7/2} & \mathbf{-5/2} & \mathbf{-3/2} & \mathbf{-1/2} & \mathbf{1/2} & \mathbf{3/2} & \mathbf{5/2} & \mathbf{7/2} \end{array} \\ \begin{pmatrix} 420 & 0 & 0 & 0 & 0 & 0 & 0 & 0 \\ 0 & -780 & 0 & 0 & 0 & 0 & 0 & 0 \\ 0 & 0 & -180 & 0 & 0 & 0 & 0 & 0 \\ 0 & 0 & 0 & 540 & 0 & 0 & 0 & 0 \\ 0 & 0 & 0 & 0 & 540 & 0 & 0 & 0 \\ 0 & 0 & 0 & 0 & 0 & -180 & 0 & 0 \\ 0 & 0 & 0 & 0 & 0 & 0 & -780 & 0 \\ 0 & 0 & 0 & 0 & 0 & 0 & 0 & 420 \end{pmatrix} \end{array} +
$$

$$
+ B_6^0 \times \begin{array}{c} \\ \mathbf{-7/2} \\ \mathbf{-5/2} \\ \mathbf{-3/2} \\ \mathbf{-1/2} \\ \mathbf{1/2} \\ \mathbf{3/2} \\ \mathbf{5/2} \\ \mathbf{7/2} \end{array} \begin{array}{c} \begin{array}{cccccccc} \mathbf{-7/2} & \mathbf{-5/2} & \mathbf{-3/2} & \mathbf{-1/2} & \mathbf{1/2} & \mathbf{3/2} & \mathbf{5/2} & \mathbf{7/2} \end{array} \\ \begin{pmatrix} 1260 & 0 & 0 & 0 & 0 & 0 & 0 & 0 \\ 0 & -6300 & 0 & 0 & 0 & 0 & 0 & 0 \\ 0 & 0 & 11340 & 0 & 0 & 0 & 0 & 0 \\ 0 & 0 & 0 & -6300 & 0 & 0 & 0 & 0 \\ 0 & 0 & 0 & 0 & -6300 & 0 & 0 & 0 \\ 0 & 0 & 0 & 0 & 0 & 11340 & 0 & 0 \\ 0 & 0 & 0 & 0 & 0 & 0 & -6300 & 0 \\ 0 & 0 & 0 & 0 & 0 & 0 & 0 & 1260 \end{pmatrix} \end{array} +
$$

$$
+ B_6^6 \times \begin{array}{c} \\ \mathbf{-7/2} \\ \mathbf{-5/2} \\ \mathbf{-3/2} \\ \mathbf{-1/2} \\ \mathbf{1/2} \\ \mathbf{3/2} \\ \mathbf{5/2} \\ \mathbf{7/2} \end{array} \begin{array}{c} \begin{array}{cccccccc} \mathbf{-7/2} & \mathbf{-5/2} & \mathbf{-3/2} & \mathbf{-1/2} & \mathbf{1/2} & \mathbf{3/2} & \mathbf{5/2} & \mathbf{7/2} \end{array} \\ \begin{pmatrix} 0 & 0 & 0 & 0 & 0 & 0 & 720\sqrt{7} & 0 \\ 0 & 0 & 0 & 0 & 0 & 0 & 0 & 720\sqrt{7} \\ 0 & 0 & 0 & 0 & 0 & 0 & 0 & 0 \\ 0 & 0 & 0 & 0 & 0 & 0 & 0 & 0 \\ 0 & 0 & 0 & 0 & 0 & 0 & 0 & 0 \\ 0 & 0 & 0 & 0 & 0 & 0 & 0 & 0 \\ 720\sqrt{7} & 0 & 0 & 0 & 0 & 0 & 0 & 0 \\ 0 & 720\sqrt{7} & 0 & 0 & 0 & 0 & 0 & 0 \end{pmatrix} \end{array} \quad (50)
$$

1.5.2 Diagonalization of the Crystal Field Hamiltonian

Combining the matrices $B_2^0O_2^0$, $B_4^0O_2^0$, $B_6^0O_2^0$ and $B_6^0O_6^0$ of Eqn. 50 gives an 8×8 matrix, which can be diagonalized in order to obtain the energies of the several states in a crystal field described by the CEF Hamiltonian Eqn. 49. All the diagonal elements correspond to contributions from O_l^m with $m = 0$, the off-diagonal elements derive from O_l^m with $m \neq 0$. The energies of the various states are then given by:

$$
\begin{aligned}
E_{11} &= 21 \cdot B_2^0 + 420 \cdot B_4^0 + 1260 \cdot B_6^0 + 0 \cdot B_6^0 \\
E_{22} &= 3 \cdot B_2^0 - 780 \cdot B_4^0 - 6300 \cdot B_6^0 + 0 \cdot B_6^0 \\
E_{33} &= -9 \cdot B_2^0 - 180 \cdot B_4^0 + 11340 \cdot B_6^0 + 0 \cdot B_6^0 \\
E_{44} &= -15 \cdot B_2^0 + 540 \cdot B_4^0 - 6300 \cdot B_6^0 + 0 \cdot B_6^0 \\
E_{55} &= -15 \cdot B_2^0 + 540 \cdot B_4^0 - 6300 \cdot B_6^0 + 0 \cdot B_6^0 \\
E_{66} &= -9 \cdot B_2^0 - 180 \cdot B_4^0 + 11340 \cdot B_6^0 + 0 \cdot B_6^0 \\
E_{77} &= 3 \cdot B_2^0 - 780 \cdot B_4^0 - 6300 \cdot B_6^0 + 0 \cdot B_6^0 \\
E_{88} &= 21 \cdot B_2^0 + 420 \cdot B_4^0 + 1260 \cdot B_6^0 + 0 \cdot B_6^0 \\
E_{71} &= 720\sqrt{7} \cdot B_6^6 \\
E_{82} &= 720\sqrt{7} \cdot B_6^6 \\
E_{17} &= 720\sqrt{7} \cdot B_6^6 \\
E_{28} &= 720\sqrt{7} \cdot B_6^6
\end{aligned}
$$

When operators of the form O_l^m with $m \neq 0$ are involved, the wave functions (or eigenvectors) may consist of linear combinations of two or more m states. The operator O_l^m mixes m states differing by m. In order to obtain the eigenstates and the eigenenergies of the above matrices, diagonalisation of the resulting 8×8 matrix has to be carried out. This, of course, has to be done by help of appropriate computer programmes. Diagonalisation rotates the coordinate axes so that the eigenvectors are no longer pure m states, but instead are linear combinations of the type $\sum a_m|m\rangle$, involving states which differ by m. The energies of the eigenstates are functions of the B_l^m.

Formally, this procedure can be outlined as follows: The application of the Hamiltonian H to the states $\Gamma = |lsjm\rangle = |m\rangle$, i.e.,

$$H|\Gamma\rangle = E|\Gamma\rangle \tag{51}$$

reveals the energy matrix

$$V_c = \langle m'|H|m\rangle \tag{52}$$

Diagonalisation of V_c is made straightforwardly employing a *unitary transformation* U, i.e.,

$$V_c^D = U^+ V_c U \tag{53}$$

yielding the eigenfunctions $|i\rangle$

$$|i\rangle = \sum_{m=-j}^{j} U_{i,m}|m\rangle \tag{54}$$

as well as the associated energy eigenvalues E_i. In a general case the eigenfunctions are mixed states of the form:

$$|i\rangle = U_{i,-j}|-j\rangle + U_{i,-j+1}|-j+1\rangle + \ldots \tag{55}$$

with $|U_{i,-j}|^2 + |U_{i,-j+1}|^2 + \ldots = 1$.

1.5.3 Point Charge Model A

Let us now consider a simple example of an Yb^{3+} ion in a crystal field produced by two negative point charges $i = 1, 2$ of $q_1 = q_2 = -0.2|e|$ situated at the positions $\vec{r}_i = (0, 0, \pm 4\text{Å})$. In this case only the γ_l^0 with $l = 2, 4, 6$ are nonzero and can be calculated according to Eqn. (20), which for the PCM can be rewritten as

$$\gamma_l^m = \frac{1}{2l+1} \sum_i \frac{q_i Z_l^m(\Omega_i)}{\epsilon_0 r_i^{l+1}} \tag{56}$$

Using the table given for the tesseral harmonic functions Z_l^m(see appendix) this gives

$$\begin{aligned}
\gamma_2^0 &= \frac{-0.2|e|}{5\epsilon_0} \sum_{i=1,2} \left(\frac{1}{4}\sqrt{\frac{5}{\pi}}[(3z_i^2 - r_i^2)/r_i^5] \right) \\
\gamma_4^0 &= \frac{-0.2|e|}{9\epsilon_0} \sum_{i=1,2} \left(\frac{3}{16}\frac{1}{\sqrt{\pi}}[35z_i^4 - 30z_i^2 r_i^2 + 3r_i^4)/r_i^9] \right) \\
\gamma_6^0 &= \frac{-0.2|e|}{13\epsilon_0} \sum_{i=1,2} \left(\frac{1}{32}\sqrt{\frac{13}{\pi}}[(231z_i^6 - 315z_i^4 r_i^2 + 105z_i^2 r_i^4 - 5r_i^6)/r_i^{13}] \right)
\end{aligned} \tag{57}$$

and inserting $z_{1,2} = \pm 4$ Å, $r_i = 4$ Å, $\epsilon_0 = 8.85419 \times 10^{-12} \frac{\text{As}}{\text{Vm}}$ and $e = 1.60217 \times 10^{-19}$ C, using (32) and looking up the Stevens factors and radial matrix elements for the Yb^{3+} ion in tables 1 and 2, respectively, the values of the crystal field parameters can be calculated.

$$\begin{aligned}
B_2^0 &= -|e|p_2^0\gamma_2^0\langle r_{4f}^2\rangle\alpha_j = 0.261\text{meV} \\
B_4^0 &= -|e|p_4^0\gamma_4^0\langle r_{4f}^4\rangle\beta_j = -1.04 \times 10^{-4}\text{meV} \\
B_6^0 &= -|e|p_6^0\gamma_6^0\langle r_{4f}^6\rangle\gamma_j = 2.81 \times 10^{-7}\text{meV}
\end{aligned} \tag{58}$$

In a similar way the crystal field parameters for pointcharges $+0.1|e|$ situated on the cornerpoints of a hexagon may be calculated. Assuming the hexagon is given by $(\pm 2\sqrt{3}, 0, 0)$ Å, $(\pm\sqrt{3}, \pm 3, 0)$ Å and $(\pm\sqrt{3}, \mp 3, 0)$ Å we obtain

$$\begin{aligned} B_2^0 &= 0.3013\text{meV} \\ B_4^0 &= 1.2 \times 10^{-4}\text{meV} \\ B_6^0 &= 3.603 \times 10^{-7}\text{meV} \\ B_6^6 &= -8.324 \times 10^{-6}\text{meV} \end{aligned} \tag{59}$$

Taking the sum of the the crystal fields produced by the charges along the z-axis (58) and on the hexagon (59) we arrive at the final result of our PCM calculation, which is summarized in table 4

Table 4: Positions of point charges and crystal field parameters for an Yb^{3+} ion in a hexagonal crystal field (model A).

pointcharges ($\|e\|$)	x(Å)	y(Å)	z(Å)
-0.2	0	0	4
-0.2	0	0	-4
0.1	3.4641	0	0
0.1	-3.4641	0	0
0.1	1.73205	-3	0
0.1	-1.73205	3	0
0.1	1.73205	3	0
0.1	-1.73205	-3	0

CEF parameters $\mathbf{B_l^m}$
$B_2^0 = 0.5622$ meV
$B_4^0 = 1.6087 \times 10^{-5}$ meV
$B_6^0 = 6.412 \times 10^{-7}$ meV
$B_6^6 = -8.324 \times 10^{-6}$ meV

Diagonalisation of Eqn. 50 taking into account the CEF parameters B_l^m as given in Table 4 reveals the eigenvalues and the eigenvectors of the problem. The following eigenvalues E_{ii}- expressed in Kelvin - with $0 \leq i \leq 8$ are derived: 138.22, 138.22, -98.6, -98.6, -59.14, -59.14, 19.54, 19.54

In general, these values are ordered such that the lowest energy is set to zero, resulting now the following sequence: 236.83, 236.83, 0., 0., 39, 46, 39.46, 118.15, 118.15.

Below, the eigenstates of these eigenvalues as derived from the diagonalisation are arranged according to the sequence of energy:

$$\begin{gathered}
0.00078|-5/2\rangle - 0.9999|7/2\rangle, \\
0.9999|-7/2\rangle + 0.00078|5/2\rangle, \\
1.|1/2\rangle, \\
1.|-1/2\rangle, \\
1.|3/2\rangle, \\
1.|-3/2\rangle, \\
-0.9999|5/2\rangle - 0.00078|7/2\rangle, \\
0.00078|-7/2\rangle + 0.9999|5/2\rangle
\end{gathered} \tag{60}$$

The knowledge of the eigenvalues and the eigenstates allows the calculation of several physical properties, which will be described in the following.

1.5.4 Calculation of the 4f-charge density for Model A

The charge density operator of a $4f$ ion is given by elementary quantum mechanics as

$$\rho_{4f}(\vec{r}) = \sum_i -|e|\delta(\vec{r} - \vec{r}_i) \tag{61}$$

Here the index i runs from 1 to the number of $4f$ electrons. Using spherical coordinates the δ-function in (61) can be rewritten

$$\delta(\vec{r} - \vec{r}_i) = \frac{1}{r^2}\delta(r - r_i)\delta(\Omega - \Omega_i) \tag{62}$$

$$\delta(\Omega - \Omega_i) = \frac{1}{4\pi}\sum_l^{\infty}(2l+1)P_l(cos\theta) \tag{63}$$

Substituting the Legendre Polynoms in (62) by spherical harmonics using the relation (16) we notice that the charge density operator can be written as a linear combination of products of spherical harmonics:

$$\rho_{4f}(\vec{r}) = -\frac{4\pi|e|}{r^2}\sum_i \delta(r - r_i)\sum_{l=0}^{\infty}\sum_{m=-l}^{l} Y_l^m(\Omega)Y_l^{m*}(\Omega_i) \tag{64}$$

In the calculation of the expectation value of the charge density operator for any $4f$ state the radial integrals yield the radial part of the $4f$ wave function:

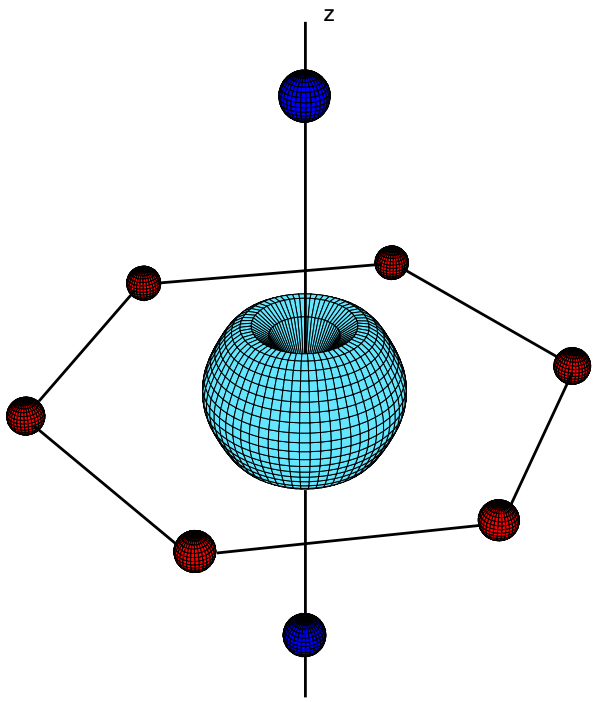

Figure 4: **Model A** $4f$-charge density for an Yb^{3+} ion surrounded by point charges (indicated by spheres) calculated at a temperature $T = 10$ K. The CEF parameters are taken from Table 4. The charges along the z-axis are $-0.2|e|$ and those in the hexagon are $0.1|e|$.

$$\langle \rho_{4f}(\vec{r}) \rangle = -4\pi|e||R_{4f}(r)|^2 \sum_{l=0}^{\infty} \sum_{m=-l}^{l} Y_l^m(\Omega) \langle \sum_i Y_l^{m*}(\Omega_i) \rangle \tag{65}$$

Keeping in mind, that the spherical harmonics are linear combinations of the tesseral harmonics according to their definition in Eqn. (18) the expectation value of the $4f$ charge density operator can be written as a linear combination of tesseral harmonics.

$$\langle \rho_{4f}(\vec{r}) \rangle = |R_{4f}(r)|^2 \sum_{lm} \sigma_l^m Z_l^m(\Omega) \tag{66}$$

According to Eqn. (65) the coefficients σ_l^m are proportional to $\langle \sum_i Z_l^m(\Omega_i) \rangle$ and can be evaluated by applying the operator equivalent method.

In order to do this we consider the product $p_l^m \Theta_l \langle r_{4f}^l \rangle \langle O_l^m \rangle$, which according to Eqn. (30) is equivalent to

$$p_l^m \Theta_l \langle r_{4f}^l \rangle \langle O_l^m \rangle = \langle \sum_i Z_l^m(\Omega_i) r_i^l \rangle \tag{67}$$

We now use the definition of Eqn. (61) to proof that

$$\langle \sum_i Z_l^m(\Omega_i) r_i^l \rangle = \frac{-1}{|e|} \int \langle \rho(\vec{r}) \rangle Z_l^m(\Omega) r^l d^3r \tag{68}$$

Inserting (66) for the charge density operator on the right side of (68), and integrating keeping in mind the orthogonality of the harmonic tesseral functions leads to

$$\frac{-1}{|e|} \int \langle \rho(\vec{r}) \rangle Z_l^m(\Omega) r^l d^3r = \frac{-1}{|e|} \langle r_{4f}^l \rangle \sigma_l^m \tag{69}$$

combining Eqns. (67) to (69) we get

$$\sigma_l^m = -|e| p_l^m \Theta_l \langle O_l^m \rangle \tag{70}$$

This yields an expression for the charge density, which may be evaluated for each crystal field state $|\Gamma_i\rangle$.

$$\langle \Gamma_i | \rho_{4f}(\vec{r}) | \Gamma_i \rangle = -|e| |R_{4f}(r)|^2 \sum_l^m p_l^m \Theta_l \langle \Gamma_i | O_l^m | \Gamma_i \rangle Z_l^m(\Omega) \tag{71}$$

Multiplying Eqn. 71 by Boltzmann factors and summing over the different CEF states, the thermal expectation value for the charge density at any temperature can be calculated. In order to visualize the charge density, usually surfaces of constant charge density are generated and plotted. Fig. 4 shows the result of the Yb^{3+} ion surrounded by the point charges producing the crystal field.

1.5.5 Calculation of magnetic moments

Magnetic moments can be evaluated for each individual CEF level and are determined by the eigenstates, the Landé factor and by the operators J_z and/or $J_\pm$. Results of such calculations impressively demonstrate why only in rare cases the observed magnetisation of a certain system coincides with the simple expression $M = g_j j$. The magnetisation is derived by evaluating the appropriate matrix elements of each CEF state.

For the $\vec{c}$ direction the magnetisation follows from $M_z = \langle \Gamma_i | J_z | \Gamma_i \rangle$, while those perpendicular to the c-axis are derived from $M_x = (1/2)\langle \Gamma_i | (J_+ + J_-) | \Gamma_i \rangle$ and $M_y = -(1/2)\mathrm{i}\langle \Gamma_i | (J_+ - J_-) | \Gamma_i \rangle$.

J_z operator In order to calculate the magnetic moment of simple and complicated eigenstates, the following procedures have to be kept in mind:

$J_z|j,m_j\rangle = m_j\hbar|j,m_j\rangle$. The magnetic moment $m_z = g_j\mu_B\langle\Gamma_i|J_z|\Gamma_i\rangle$ follows then simply from $m_z = g_j\mu_B\langle j,m_j|J_z|j,m_j\rangle$.

Example Considering the eigenstate $|5/2,3/2\rangle$ and $g_j = 6/7$:
$m_j = g_j\mu_B\langle 5/2,3/2|J_z|5/2,3/2\rangle = g_j\mu_B(3/2)\langle 5/2,3/2||5/2,3/2\rangle = g_j(3/2)\delta_{i,j} = 6/7\mu_B\cdot 3/2\cdot 1 = 1.285\mu_B$

Ladder operators Definition: $J_\pm = J_x \pm \mathrm{i}J_y$

$J_\pm|j,m_j\rangle = \hbar\sqrt{j(j+1)-m_j(m_j\mp 1)}|j,m_j\pm 1\rangle$. The magnetic moment follows then via $m_\pm = g_j\mu_B\langle\Gamma_i|J_\pm|\Gamma_i\rangle$.

Example Considering the eigenstate $|5/2,3/2\rangle$ and $g_j = 6/7$:
$m_j = g_j\mu_B\langle 5/2,3/2|J_+|5/2,3/2\rangle =$
$g_j\mu_B\sqrt{5/2\cdot 7/2 - 3/2\cdot 5/2}\langle 5/2,3/2||5/2,5/2\rangle = g_j\mu_B\sqrt{5}\delta_{i,j} = 2.23\mu_B\cdot 0 = 0\mu_B$.

In order to obtain a finite magnetisation, states like $\langle 5/2,3/2||5/2,1/2\rangle$ or $\langle 5/2,5/2||5/2,3/2\rangle$ or $\langle 5/2,1/2||5/2,-1/2\rangle$ have to be combined. Very frequently, the actual wave function does not provide such eigenstates; therefore the magnetic moments derived from the $J_\pm$ operators become zero. The above example would give a magnetic moment only in the case
$m_j = g_j\mu_B\langle 5/2,5/2|J_+|5/2,3/2\rangle = g_j\mu_B\cdot\sqrt{5/2\cdot 7/2 - 3/2\cdot 5/2}\langle 5/2,5/2||5/2,5/2\rangle = g_j\sqrt{5}\delta_{i,j} = 2.23\mu_B\cdot 1 = 2.23\ \mu_B$.

Magnetic moments of model A As an example, we calculate the magnetisation of the ground state of a hexagonal Yb compound, i.e., of the CEF level with lowest energy as derived by the CEF parameters given in Table 4. $M_z = g\mu_B(\langle 1/2|J_z|7/2\rangle = 6/7\mu_B\cdot 0.5\delta_{ij} \approx 0.428\ \mu_B$ The first eigenstate at 39.46 K with eigenfunction $|\pm 3/2\rangle$, reveals a moment $\pm 1.28\ \mu_B$. Since both states have the same energy, they are two-fold degenerate. The application of a small external field would split the CEF states lifting therefore this degeneracy. Results of the magnetic moments associated with the various CEF states are summarised in Table 5.

1.5.6 Effect of magnetic field on the charge density - a source of Magnetostriction

The application of a magnetic field gives also rise to a change in the $4f$ charge density, which in turn may lead to magnetostriction. In order to demonstrate this effect we show in fig. 5 the charge density of the Yb^{3+} ion in an applied magnetic field of 40 T along the y axis.

Table 5: Magnetic moments of an Yb^{3+} ion exposed to CEF effects described by the CEF parameters in Table 4

energy level [K]	M_z μ_B	M_+ μ_B	M_- μ_B
0	-0.42	1.71	-1.71i
0	0.42	1.71	-1.71i
39.46	-1.28	0	0
39.46	1.28	0	0
118.15	2.14	0.0017	-0.0017i
118.15	-21.14	0.0017	0.0017i
236.83	-3	-0.0017	0.0017i
236.83	3	-0.0017	-0.0017i

Table 6: Positions of point charges and crystal field parameters for an Yb^{3+} ion in a hexagonal crystal field (Model B).

pointcharges ($\|e\|$)	x(Å)	y(Å)	z(Å)
0.8	0	0	3
0.8	0	0	-3
0.8	3.4641	0	0
0.8	-3.4641	0	0
0.8	1.73205	-3	0
0.8	-1.73205	3	0
0.8	1.73205	3	0
0.8	-1.73205	-3	0

CEF parameters $\mathbf{B_l^m}$
$B_2^0 = -0.06364$ meV
$B_4^0 = 2.713 \times 10^{-3}$ meV
$B_6^0 = -5.5335 \times 10^{-6}$ meV
$B_6^6 = -6.659 \times 10^{-5}$ meV

1 meV = 11.6 K
B20 = -0.7388 K
B40 = 0.0315 K
B60 = -6.4237E-5 K
B66 = - 7.7302E-4 K

1.5.7 Point Charge Model B

In order to show, how changes of the point charges influence the experimental results, we evaluate also another model, with different sign and distance of point charges situated on the hexagonal axis. The point charges and the resulting crystal field parameters are summarized in table 6.

Diagonalizing the Hamiltonian in a similar manner as was done in Eqn. 50, the eigenstates and the eigenvalues are derived for the CEF parameters outlined in Table 6. Model B yields a rather narrow splitting with doublets at 0, 24.24, 26.86 and 55.3 K. The magnetic moment of the ground state doublet $-0.995|-5/2\rangle - 0.0306|7/2\rangle$

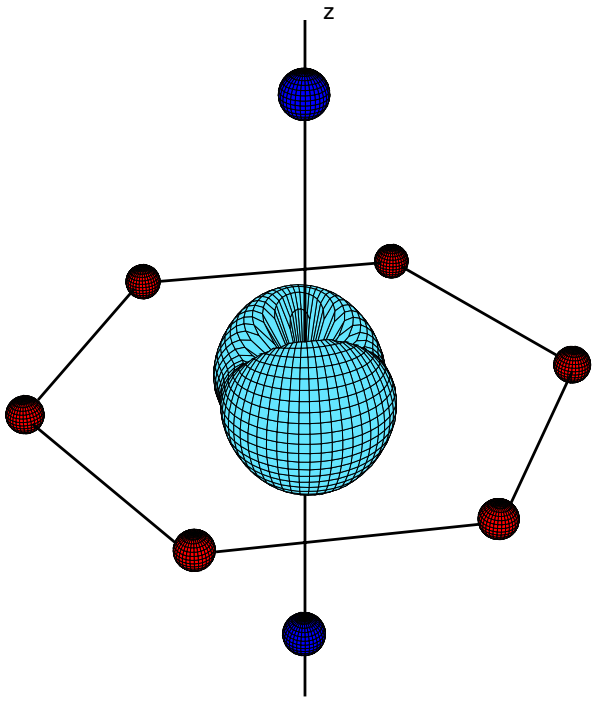

Figure 5: Model A: $4f$-charge density for Yb^3+ surrounded by point charges indicated by the spheres calculated at a temperature $T = 10$ K and applied 40 T magnetic field along (010).

and $0.995|5/2\rangle + 0.0306|-7/2\rangle$ associated with J_z amounts to $\pm 2.138\ \mu_B$. Note the significant changes in both the overall splitting and the magnetic moment of the ground state driven by the changes of the point charges. The small separation between the first and the second excited level gives rise to the appearance of a so called quasi-quartet.

2 Physical properties and CEF effects

In the following section we will discuss a number of physical properties, which cannot be explained unless crystalline electric field effects are considered.

Two different scenarios have to be taken into account:

- Properties depend only on the degeneracy of the various CEF states. Examples here are the specific heat or magnetic entropy.
- Properties depend on the degeneracy and on the matrix elements between a certain CEF level an on the matrix elements between various CEF states, e.g.,

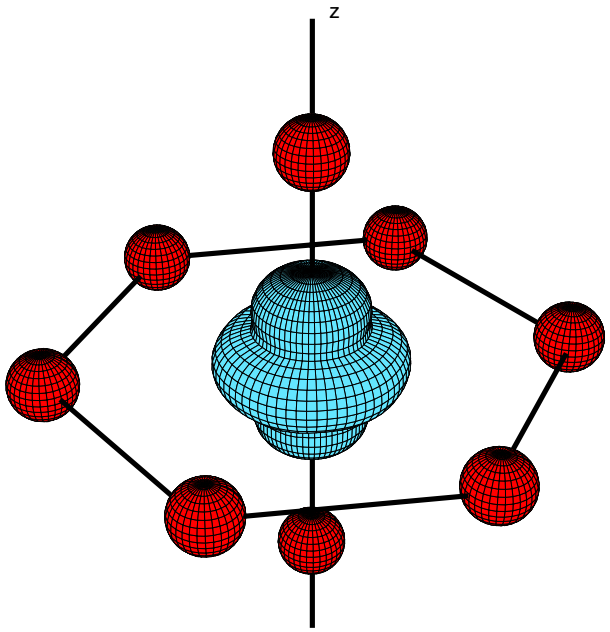

Figure 6: Model B: $4f$-charge density for an Yb^3+ ion surrounded by point charges indicated by the spheres calculated at the temperature $T = 10$ K. The CEF parameters are taken from Table 6. The charges along the z-axis and in the hexagon are $0.8|e|$.

electrical resistivity, magnetic susceptibility, isothermal magnetisation, inelastic neturon scattering cross section.

2.1 Neutron inelastic scattering

The neutron powder cross section (unpolarized neutrons) for each crystal field transition (in [barn/ion/sr]) at a given temperature can be expressed as [14]:

$$\begin{aligned}\frac{d\sigma_{i\to k}}{d\Omega} &= \frac{k_f}{k_i}\{\frac{1}{2}g_j F(Q)\}^2 exp(-2W)\left(\frac{\hbar\gamma e^2}{mc^2}\right)^2 \frac{exp(-E_i/k_BT)}{\sum_j exp(-E_j/k_BT)} \times \\ &\quad \times\frac{2}{3}\sum_{\alpha=x,y,z}|\langle i|J^\alpha|k\rangle|^2 \end{aligned} \tag{72}$$

with the form factor $F(Q)$ (giving there is a Q dependence), the ratio k_f/k_i of the outgoing and incoming wave vector of the neutrons and the Debye Waller factor $\exp(-2W(Q))$

Taking into account model A with the CEF parameters given in Table 4, both the eigenvalues and the eigenstates are derived after diagonalising the appropriate Hamiltonian (see Eqn. 50). While the former define the energy separation between

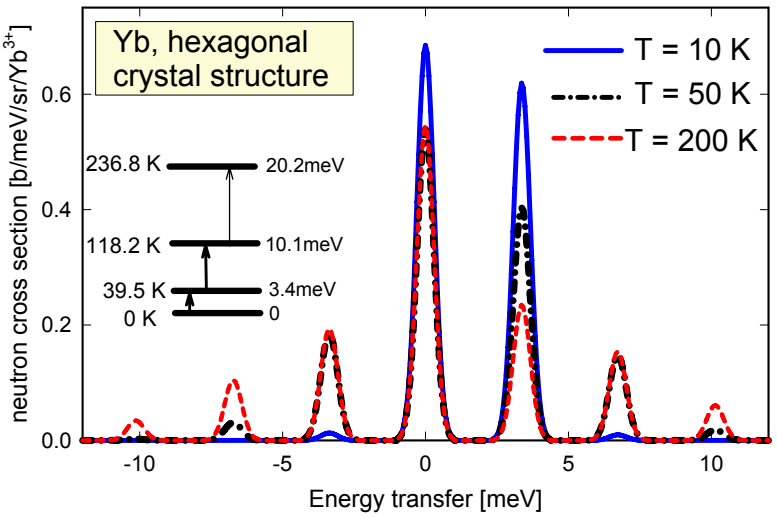

Figure 7: Calculated neutron spectra at different temperatures for the Yb^{3+} ion in a hexagonal crystal field according to model A. The inset shows the calculated crystal field level scheme, arrows indicate strong transition matrix elements.

levels, the latter allow to calculate the matrix elements within a certain CEF multiplet and between the various levels. Carrying out these calculations according to Eqn. 72 and convolute the derived data with a gaussian resolution function gives calculated neutron inelastic neutron (NIS) spectra for the hexagonal Yb compound in terms of model A as shown in Fig. 7. At low temperature only one transition can be seen, from the ground state to the first excited level. All other matrix elements in Eqn. 72 are zero, hence no intensity is observed. Increasing the temperature populates thermally excited CEF states and the neutrons can induce further transitions between excited states as can be seen in Fig. 7.

2.2 The Schottky contribution to the specific heat

The so called Schottky contribution to the specific heat is originated from the thermal population of the various crystal field levels and thus results from the increase of the free energy of the system.

$$F = \frac{R \sum_{r=0}^{m} \Delta_r g_r \exp\left(\frac{-\Delta_r}{k_B T}\right)}{\sum_{r=0}^{m} g_r \exp\left(\frac{-\Delta_r}{k_B T}\right)} \tag{73}$$

g_r is the degeneracy of the r-th level, Δ_r the energy difference to the ground state and R the gas constant ($R = 8.314$ J/molK).

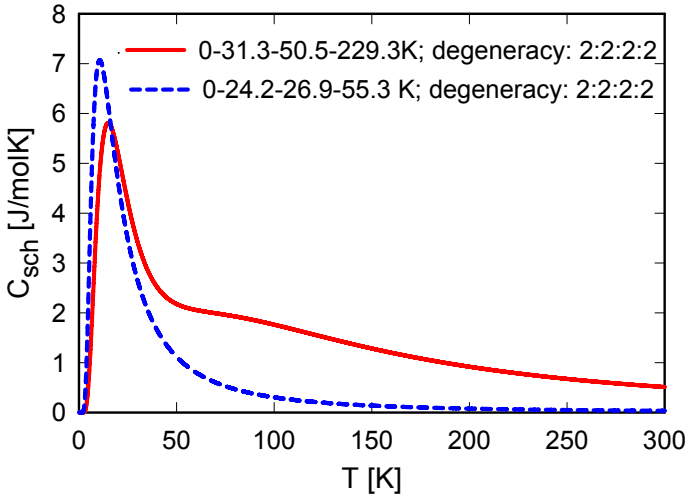

Figure 8: Temperature dependent specific heat corresponding to a hexagonal Yb compound calculated for the CEF parameters of model A (Table 4) and model B (Table 6. The sequence of numbers gives the respective CEF splitting and the degeneracy.

The specific heat can then be calculated from Eqn. 73 employing

$$C_{V,P} = -T\frac{\partial^2 F(T)}{\partial T^2}|_{V,P} = T\frac{\partial^2 (k_B T \ln Z)}{\partial T^2}|_V \tag{74}$$

where the partition function Z is defined as $F = -k_B T \ln Z$. Z represents the accessible states at a given temperature, hence, the calorimetric technique can be considered as a type of *thermal spectrocopy*. There, the heat dQ is the exciting energy absorbed by the system. The initial state is characterised by the temperature T_i and the final one by $T_f = T_i + \mathrm{d}T$. The system remains in its final state, because it is always in thermal equilibirium [11].

For solids, the heat capacity taken at constant pressure equals about that taken at constant volume, i.e., $C_P \approx C_V$.

Fig. 8 shows the crystal field contribution to the specific heat for a typical set of CEF level splittings and typical values of the degeneracy of each level.

In particular, a 2-level system is simply described by:

$$C_{Sch} = \frac{R\left(\frac{\Delta}{k_B T}\right)^2 g \exp\left(\frac{\Delta}{k_B T}\right)}{\left(1 + g\exp\left(\frac{-\Delta}{k_B T}\right)\right)^2}. \tag{75}$$

There, g is the ratio of the the excited level to that of the ground state. Some general trends of the crystal field contribution of 2-level systems are summarised in table 7. If the levels are well separated, the maximum in the specific heat appears *roughly* at half of the splitting of the states.

Table 7: Temperature T_{max} of the maximum of the Schottky anomaly c_{Sch} and entropy as a function of the degeneracy ratio g and crystal field splitting Δ [11].

excitation	g	c_{Sch}^{max} [J/molK]	T_{max}/Δ	entropy
Quartett → Dublett	0.5	2.00	0.448	$R\ln(3/2)$
Dublett → Dublett	1	3.64	0.417	$R\ln 2$
Dublett → Quartett	2	6.31	0.377	$R\ln 3$

2.3 Magnetic entropy

Magnetic entropy is one of the most important physical quantities and can be derived without the application of models and approximations. The magnetic entropy measures the degrees of freedom of a particular spin system. In the most simplest scenario, an electron spin 1/2 has two degrees of freedom, i.e, spin↑, and spin↓. The entropy associated with the lifting of the degeneracy of these degrees of freedom derives from the well known Boltzmann statistics and amounts to $S_{mag} = R\ln 2$.

From thermodynamics it is well known that the entropy S is defined as $S = k_B \ln Z$ and can be derived by integrating C_{mag}/T, i.e.,

$$S_{mag}(T) = S_0 + \int \frac{C(T)}{T} \mathrm{d}T. \tag{76}$$

Fig. 9 shows the magnetic entropy for both, model A and model B. Due to the much smaller overall CEF splitting, $R\ln 4$ is recovered at much lower temperatures than the entropy of of model A, where $R\ln 4$ is not regained well below room temperature. If $S_{mag}(T)$ exhibits regions with plateau-like dependences, a substantial splitting is expected between levels and a steady increase of $S_{mag}(T)$ refers to relatively narrow distances between levels.

In a very general manner, the entropy well above a certain CEF level follows from $R\ln(N_o/N_g)$ where N_o is the number of states states already populated and N_g is the ground state degeneracy. Having populated e.g., 3 CEF doublets would result in $N_o = 6$ and in the case of 4 doublets, coinciding with Yb in a hexagonal CEF, $N_o = 8$. The entropy for the former is then $R\ln(6/2) = R\ln 3$, while for the latter one observes $R\ln(8/2) = R\ln 4$, in agreement to the results of Fig. 9.

It is important to note that a contribution of a ground state doublet to the specific heat and thus also to the magnetic entropy, depends on the availability of external mechanisms, lifting the ground state degeneracy. Such mechanisms may be the Kondo effect, long range magnetic order or a crystal distortion which lowers the symmetry. A doublet as ground state *does not* automatically contribute $R\ln 2$ to the entropy. Only mechanisms like those indicated above, will generate entropy for this level!

Let us assume a Kondo interaction strenght of $T_K = 5$ K as typical figure of Yb intermetallics. As indicated above, this phenomenon lifts the degeneracy of the ground

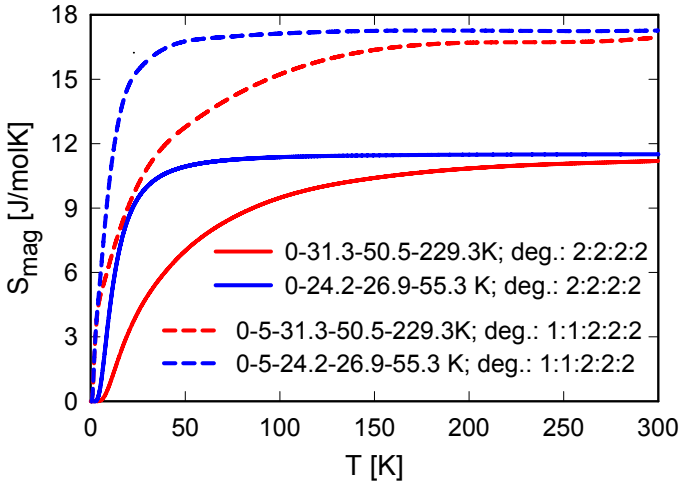

Figure 9: Temperature dependent magnetic entropy S_{mag} corresponding to a hexagonal Yb compound calculated for the CEF parameters of model A (Table 4) and model B (Table 6), solid lines. The dashed lines represent the magnetic entropy after lifting the ground state degeneracy by Kondo interaction with $T_K = 5$ K. The sequence of numbers gives the respective CEF splitting and the degeneracy.

state doublet and $R \ln 2$ is regained for $T \gg T_K$. Applying the Kondo effect to both data sets in Fig. 9 shows that at sufficientyl high temperatures $R \ln 8$ is recovered.

Fig. 10 shows the magnetic contribution to the specific heat of one of the best studied Pr compounds, i.e, $PrNi_5$. This hexagonal compound does not show magnetic order, although the total angular momentum $j = 4$ of Pr^{3+} refers to a magnetic moment $M = g_j j = 3.2\ \mu_B$, in fact, a very large moment. The reason for the nonmagnetic ground state is CEF splitting on the non-Kramers ion Pr^{3+}, with the possibility to create non-magnetic CEF states. The expression *nonmagnetic* should be considered with care: In CEF physics nonmagnetic means that the sum of the matrix elements of a certain state becomes zero. We will come back to this scenario in the chapter concerning magnetization and susceptibility. The relevant CEF parameters B_l^m of $PrNi_5$ are $B_2^0 = 5.84$ K, $B_4^0 = 4.53 \times 10^{-2}$ K, $B_6^0 = 8.86 \times 10^{-4}$ K, $B_6^6 = 3.14 \times 10^{-2}$ K.

Diagonalizing the appropriate Hamiltonian (a 9×9 matrix) reveals the following eigenvalues (in bracket is the degeneracy), numbers are rounded. $E_i = 0\ K[1]$, $24\ K[1]$, $40\ K[2]$, $49\ K[2]$, $158\ K[1]$, $333\ K[2]$.

The eigenstates corresponding to these eigenvalues and the magnetic moments associated are (in rounded numbers): $0.71|-3\rangle + 0.71|+3\rangle$, $[0\ \mu_B]$; $1|0\rangle$, $[0\ \mu_B]$; $1|1\rangle$, $[-0.8\ \mu_B]$; $1|-1\rangle$, $[0.8\ \mu_B]$; $-0.97|-2\rangle + 0.21|+4\rangle$, $[1.38\ \mu_B]$; $0.21|-4\rangle - 0.97|+2\rangle$, $[-1.38\ \mu_B]$; $0.71|-3\rangle + 0.71|+3\rangle$, $[0\ \mu_B]$; $0.97|-4\rangle + 0.21|+2\rangle$, $[2.98\ \mu_B]$; $0.21|-2\rangle + 0.97|+2\rangle$, $[-2.98\ \mu_B]$.

The anomaly in specific heat at low temperatures is purely of CEF origin and should

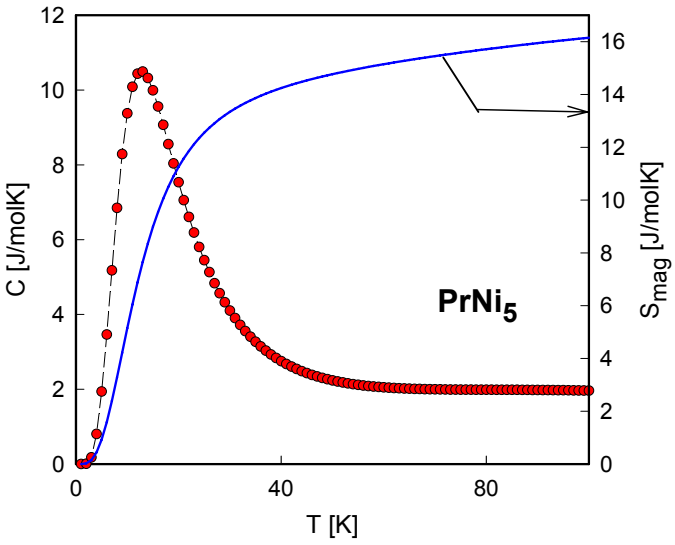

Figure 10: Calculated temperature dependent specific heat C (left axis) and temperature dependent magnetic entropy S_{mag} (right axis) of $PrNi_5$. The CEF parameters are given in the text.

not be confused with certain classes of phase transitions.

2.4 Magnetisation and magnetic susceptibility

To calculate magnetic properties of a single rare earth ion subjected to both the crystal field and a magnetic field, H_i^{eff}, the the crystal field and Zeeman Hamiltonian (77) of the ion i has to be diagonalized together:

$$\mathcal{H} = B_l^m O_l^m(\mathbf{J}_i) - g_{Ji}\mu_B \mathbf{J}_i \mathbf{H}_i^{eff}. \tag{77}$$

It allows to calculate the expectation value of the angular momentum $\langle \mathbf{J}_i \rangle$ according to

$$\langle \mathbf{J}_i \rangle = \sum_\Gamma n_\Gamma \langle \Gamma | \mathbf{J}_i | \Gamma \rangle \tag{78}$$

with

$$n_\Gamma = \frac{\exp(-E_\Gamma/kT)}{z} \tag{79}$$

$$z = \sum_\Gamma \exp(-E_\Gamma/kT) \tag{80}$$

The operator $\boldsymbol{J}_i$ represents J_z and $J_\pm$; z is the partition sum, $|\Gamma\rangle$ the eigenstate corresponding to the eigenvalue E_Γ of the Hamiltonian (77).

2.4.1 Isothermal Magnetisation

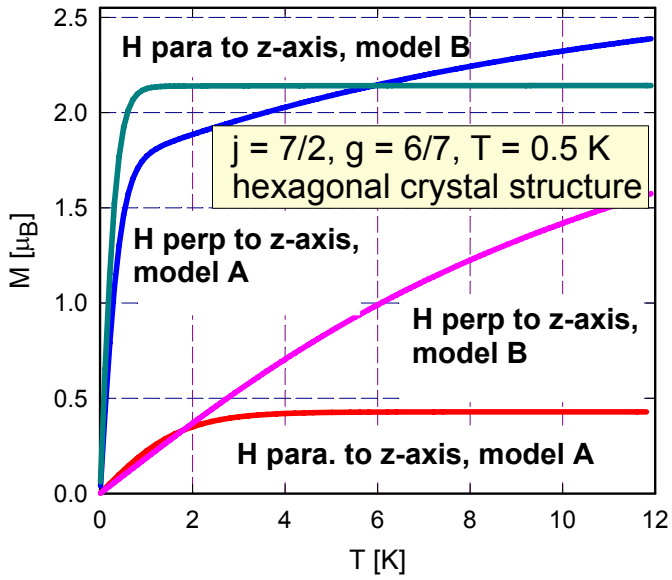

Figure 11: Isothermal magnetization of an Yb compound ($j = 7/2$) with hexagonal crystal structure at $T = 0.5$ K for CEF parameters of model A (Table 4) and model B (Table 6.

We have shown in Section 1.5.5 how a magnetic moment of a certain eigenstate can be calculated. In most of the cases, however, the eigenstates may become quite com plicated, consisting of a linear combination of the $|\pm 1/2\rangle$, $|\pm 1\rangle$, $|\pm 3/2\rangle$ ..., i.e, $\alpha|\pm 1/2\rangle + \beta|\pm 1\rangle + \gamma|\pm 3/2\rangle$ .... Formally, $(\alpha + \beta + \gamma + \ldots)^2 = 1$. α, β ... can be both positive and negative. The matrix elements of all individual states have to be summed up to generate the total magnetic moment of the system with respect to a certain direction of the external magnetic field. Mathematically this follows from

$$m_i = g_j \mu_B \langle \Gamma_i | J_i | \Gamma_i \rangle. \quad (81)$$

This value has to be calculated at each temperature and each field. Temperature also causes that higher levels of the CEF scheme become populated and thus contribute to the mean value of m_i.

Examples of isothermal magnetisation curves are shown in Fig. 11 for the hexagonal Yb compound with CEF parameters given in Table 4 for model A and in Table 6 for

model B. Note that CEF splitting is responsible that the expected value $M = g \cdot j$ is not reached unless very high external magnetic fields are applied which are different for the different directions of the crystal.

The magnetic field not only causes a polarisation against thermal disorder, but further splits degenerate levels. A triplet, for example, is lifted into 3 singlets according to Zeeman's law.

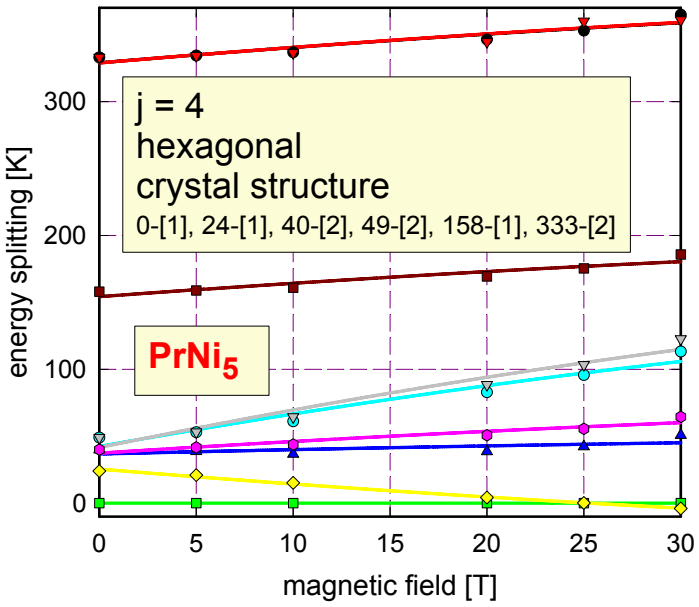

Figure 12: Field dependence of the $PrNi_5$ eigenstates. Note the lifting of the degeneracy of states and the level crossing at about 24 T. The sequence of numbers refer to the energies of the levels in Kelvin (rounded) and the number in brackets is the degeneracy both at zero external fields.

A rather exciting phenomenon in this context is so called *level crossing*, see Fig. 12. This means, that while certain levels are shifted to higher energies as the field strength increases, others become lowered. A consequence can be that a level with a large magnetic moment is lowered, finally crossing the split levels of the ground state. Isothermal magnetisation can then exhibit sharp, field induced changes of the magnetic moment. A very famous example is already mentioned $PrNi_5$, and field dependent calculations of the isothermal magnetisation are shown in Fig. 13, exhibiting a metamagnetic-like transition around 23 T, well in agreeement to experimental results. Slight changes of the B_l^m however, can cause dramatic changes of this transition. In real materials, however, interactions between ions may occur, which may modify final results.

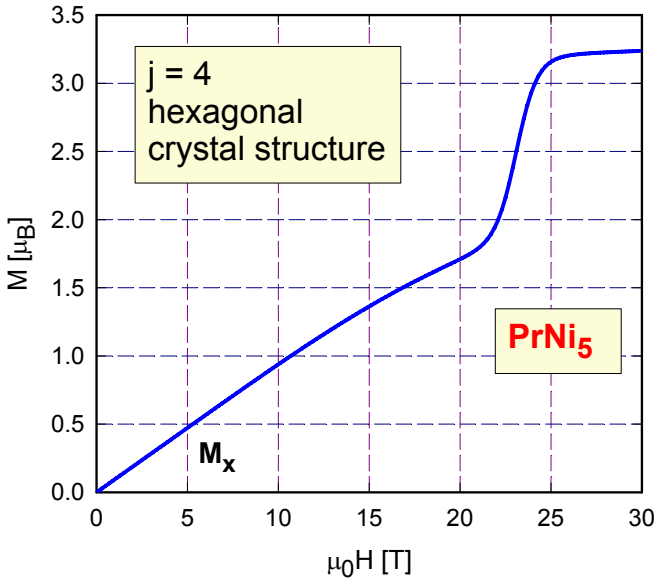

Figure 13: Field dependent magnetisation of $PrNi_5$ with fields applied along the $\boldsymbol{x}$-direction calculated at $T = 0.5$ K.

2.4.2 Temperature dependent susceptibility

When a magnetic field is applied along the direction α, the magnetic susceptibility χ_α^{CEF} follows from the Van Vleck formula and can be expressed as [12],

$$\begin{aligned} \chi_\alpha^{CEF} &= \frac{N_{\rm A}(g_j\mu_B)^2}{\sum_n \exp(-E_n/k_BT)} \times \\ &\times \sum_{r,s} |\langle r|J_\alpha|s\rangle|^2 \exp\left(\frac{-E_r}{k_BT}\right) \frac{\exp((E_r-E_s)/k_BT)-1}{E_r-E_s}. \end{aligned} \tag{82}$$

N_A is the Avogadro number, E_r is the energy of the r-th state, g_j is the Landé factor and $\langle r|J_\alpha|s\rangle$ is the matrix element between the r- and s-state of a CEF scheme.

The magnetic susceptibility $\chi(T)$ as outlined in Eqn. 83 modifies the the simple Curie law by taking into account both, the matrix elements between the different states of a CEF split total angular momentum as well as the probability that a certain CEF level is populated at a distinct temperature. Results of calculations for the hexagonal $j = 7/2$ compound, model A, are shown in Fig. 14 for fields applied in the basal plane and along the c-axis, respectively. The sum of both contributions, i.e., $\chi = 1/3\chi_{para} + 2/3\chi_{perp}$ corresponds to a measurement performed on polycrystalline materials. At very high temperatures, the slope of the averaged curve coincides with the effective moment $\mu_{eff} = 4.54\ \mu_B$ of a free, trivalent Yb ion.

Fig. 15 shows the calculated temperature dependent susceptibility of $PrNi_5$. Note

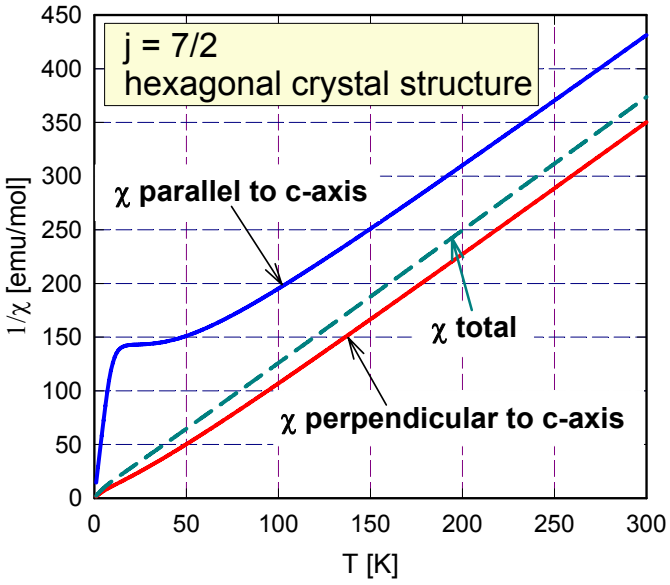

Figure 14: Temperature dependent magnetic susceptibility χ of an Yb compound ($j = 7/2$), model A, with hexagonal crystal structure plotted as $1/chi$ vs. T calculated for both field directions, i.e., $H//\boldsymbol{c}$ and $H \perp c$. The doublet CEF states are at 0, 31.3, 50.5, and 229.2 K. The sum curve, $\chi_{tot} = 1/3\chi_c + 2/3\chi_a$ reveals at high temperatures the effective magnetic moment of Yb^{3+}, $\mu_{eff} = 4.54\ \mu_B$.

that the $1/\chi$ plot for both directions has finite values at $T = 0$. This refers to a nonmagnetic ground state - in contrast to the previous Yb compound - as a result of CEF effects exerted to the non-Kramers ion Yb. If the ground state is magnetic, $1/\chi$ would diverge. Moreover, $1/\chi$ exhibits strongly curved temperature dependences and thus deviates from the simple Curie-like behaviour, i.e., $1/\chi \propto T$.

2.5 Electrical resistivity

Scattering of electrons on ions bearing a permanent magnetic moment consists of contributions due to the standard (spherical) potential, but there is additionally the interaction of the conduction electron spin with the magnetic moment of the ion.

Scattering can be elastic or inelastic; in both cases, the scattering cross section and thus the efficiency of scattering is different for spin↑ and spin↓ electrons.

If only local magnetic moments are considered, as it is almost perfectly the case for the $4f$ moments of the rare earth elements, a perturbation type calculation in the scope of the Heisenberg model

$$H = -\mathcal{J} \cdot \vec{S} \cdot \vec{s} \tag{83}$$

can be done. To be more specific, we assume that the exchange interaction between the

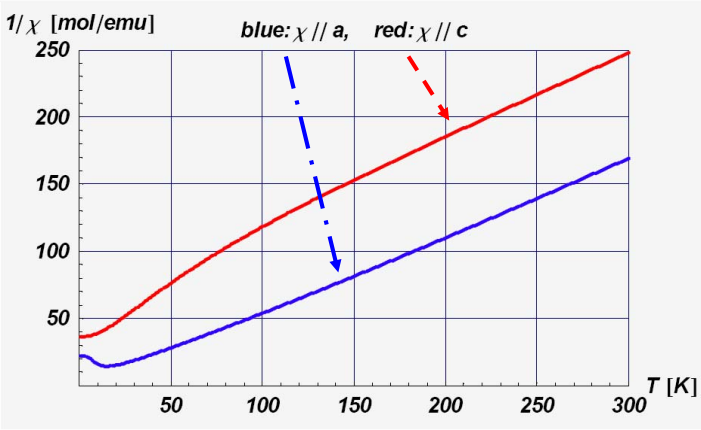

Figure 15: Temperature dependent magnetic susceptibility of $PrNi_5$ calculated for both field directions, i.e., $H//\boldsymbol{c}$ and $H \perp c$. The sum curve, $\chi_{tot} = 1/3\chi_c + 2/3\chi_a$ reveals at high temperatures the effective magnetic moment of Pr^{3+}, $\mu_{eff} = 3.58\ \mu_B$.

conduction electron at the site $\vec{r}$ with spin $\vec{s}$ and the localized magnetic ion at the site $\vec{R}$ with spin $\vec{S}$ is of importance only, if the conduction electron is in the proximity of the magnetic ion. This mathematically means one uses a δ-function, i.e., the potential of the interaction reads

$$V(\vec{r}) = -\mathcal{J}\delta(\vec{r} - \vec{R})\vec{s}\vec{S}(1/\hbar^2).$$

where $\mathcal{J}$ is the exchange integral or exchange constant ($\mathcal{J}$ has the dimension *energy* $\times$ *volume*). With $\vec{j} = l + S$ it follows that $\vec{S} = (g-1)\vec{j}$. Within the standard notation, g is the Landé-factor and j the total angular momentum. Thus

$$V(\vec{r}) = -(1/\hbar^2)\mathcal{J}(g-1)\delta(\vec{r} - \vec{R})\vec{s}\vec{j}. \tag{84}$$

Note that $\vec{s}\vec{j}$ can be written as

$$\vec{s}\cdot\vec{j} = s_z J_z + \frac{1}{2}(s_+ J_- + s_- J_+)$$

A conduction electron in the state $\vec{k}$ moving in the vicinity of the magnetic ion is scattered by the potential given in Eqn. 84 into a new state $\vec{k}'$. The scattering occurs without spin flip if the initial and the final state are connected by $s_z J_z$, but a spin flip occurs if they are connected by the terms $s_\pm J_\pm$ [13]. The scattering probability is proportional to the absolute square of matrix elements $M_{ii'}(\vec{k} \rightarrow \vec{k}')$ connecting initial (i) and final (i') states of the system.

The electrical resistivity ρ, following the *Drude model* can be expressed as

$$\rho = \frac{3\pi^2 m}{e^2 k_F^3}\frac{1}{\tau(\epsilon)}$$

where m is the charge carrier mass, e the electron charge, k_F the Fermi wave vector and $\tau(\epsilon)$ the relaxation time. Textbooks on *Transport phenomena* demonstrate that

$$\begin{aligned}\frac{1}{\tau_\pm} &= \frac{mk_F}{\pi\hbar^3}[\sum_{i,i'} N_i|M_{ii'}(\vec{k}_\pm \rightarrow \vec{k}'_\pm|^2 \frac{2}{1+\exp(-E_{ii'}/k_BT)} \\ &+ \sum_{j,j'} N_j|M_{jj'}(\vec{k}_\pm \rightarrow \vec{k}'_\mp|^2 \frac{2}{1+\exp(-E_{jj'}/k_BT)}]\end{aligned} \tag{85}$$

where $\tau_\pm$ are the relaxation times for spin up (+) and spin down (-) electrons; $E_{ii'}$ and $E_{jj'}$ are the energies gained by the electrons in the particular scattering process. N_i and N_j are the number of scattering centers per unit volume producing the collision processes.

In the absence of electric and magnetic fields, all the m_j substates are degenerate and thus they are equally probable. $E_{ii'} = E_{jj'} = 0$ since all collisions are elastic.

The electrical resistivity for the paramagnetic temperature range $T > T_{ord}$ is then calculated from:

$$\rho_{mag}(T) = \frac{3\pi N m^*}{2\hbar e^2 \epsilon_F}|\mathcal{J}|^2 \frac{1}{4}(g_j-1)^2 \cdot j(j+1), \tag{86}$$

indicating a temperature independent expression. For $T > T_{ord}$ the spins are independently from each other. ρ_{mag} is determined by the so called deGennes-factor $(g_j-1)^2 \cdot j(j+1)$, the coupling constant $\mathcal{J}$ and the effective mass m^* of the charge carriers.

Crystal electric fields modeled by the potential V_c, however, cause that scattering can happen in more "channels", represented by the various multiplets which are created by the regularly arranged charges around the magnetic ions. This causes an increase of the spindisorder resistivity as more and more levels become active (i.e., populated) as the temperature increases. If the level splitting is large and the actual temperature is well in-between, $\rho_{mag}(T)$ may become again temperature independent.

The matrix elements $M_{ii'}$ and $M_{jj'}$ have now to be taken between the different CEF states. The probability p_i of a magnetic ion being in a certain CEF state with energy E_i follows via the Boltzmann statistics from

$$p_i = \frac{N_i}{N} = \frac{\exp(-E_i/k_BT)}{\sum_j \exp(-E_j/k_BT)}.$$

The transition between different states refers to inelastic scattering, hence, the $E_{ii'}$ and $E_{jj'}$ will not all be zero.

Altogether, adding the CEF effect to Eqn. 86, the electrical resistivity in presence of CEF splitting becomes modified and may be expressed as

$$\rho_{spd}(T) = \frac{3\pi N m}{\hbar e^2 \epsilon_F}\mathcal{J}^2(g_j-1)^2 \sum_{m_s,m'_s,i,i'} \langle m'_s i'|\vec{sj}|m_s i\rangle^2 p_i f_{ii} \tag{87}$$

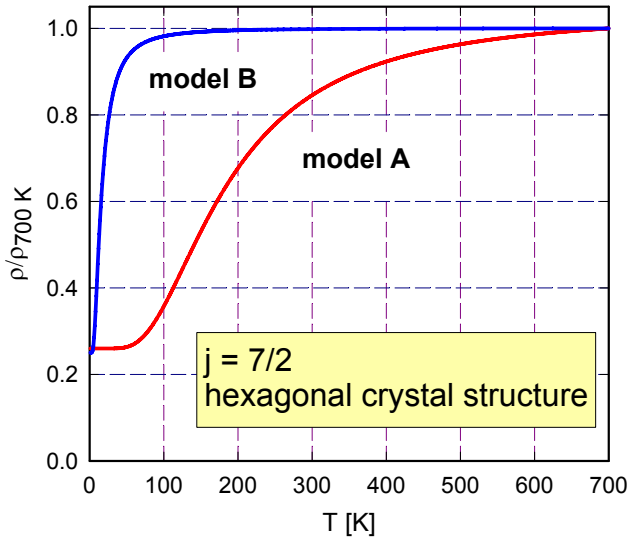

Figure 16: Electrical resistivity of an Yb compound ($j = 7/2$) in a hexagonal crystal structure for CEF parameters of model A (Table 4) and model B (Table 6.

m_s and m'_s are the spins of the conduction electrons in the initial and the final states. i and i' are the CEF states with energies E_i and E'_i. The matrix elements are between the simultaneous eigenstates for the local-moment-conduction-electron system; the f_{ii} are given by

$$f_{ii'} = \frac{2}{1 + \exp[-(E_i - E'_i)/k_B T]}.$$

Note that similarly to the case of inelastic neutron scattering transition probabilities between CEF states are of importance. Standard selection rules are such that matrix elements have finite values only if $m_j \rightarrow m_j \pm 1$ (dipole exchange selection). If such states are not available, scattering between these states will not occur, hence does not contribute to the electrical resistivity. For temperatures high compared to the overall CEF splitting, Eqn. 86 is recovered, resulting in a temperature independent expression.

Fig. 16 shows the remarkable influence of CEF effects on the the spindisorder resistivity. Data from the previous hexagonal Yb compounds, model A and B are used. The thermal population in the context of transition probabilities between CEF states at different CEF levels originates a strong temperature dependence, which *should not* be confused with e.g., T^2 dependences derived from Fermi liquid behaviour or similar interactions!

In order to demonstrate the influence of the degeneracy of a CEF level regarding the electrical resistivity, a simple example of an $j = 5/2$ in cubic symmetry is shown in Fig. 17. A quartet as ground state, in comparison to the doublet, causes a higher scattering rate, hence the resistivity for $T \rightarrow 0$ is larger, as obvious from Fig. 17. Since

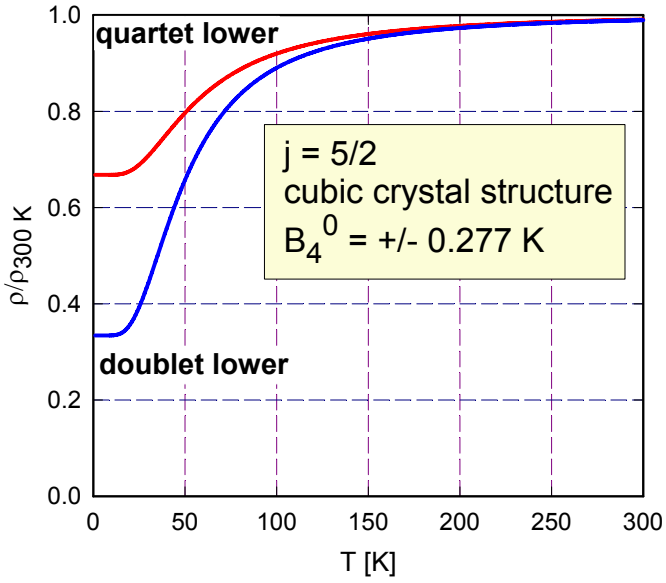

Figure 17: Electrical resistivity of a cerium compound ($j = 5/2$) in cubic environment. $B_4^0 = \pm\Delta/360$ [K] with $\Delta = 100$ K.

there, the overall CEF splitting $\Delta = 100$ K, the resistivity around room temperature becomes almost constant.

3 Thermal Expansion and Magnetostriction

As pointed out already in the context of the Yb example, the change of temperature and magnetic field will lead to a change in the charge density of the $4f$ electrons, which in turn will influence the lattice. Fig. 18 shows the basic mechanism [15] for a simple example.

A crystal field produced according to Coulomb's law by two positive charges (situated above and below the rare earth). For temperatures higher than the crystal field splitting Δ_{cf} of the $4f$ ground state multiplet the $4f$ charge density is spherical symmetric (Fig. 18a left). When the temperature is lower than the crystal field splitting, only the low energy crystal field states are thermally populated. This leads to a continuous deformation of the $4f$ charge density with decreasing temperature. The shape of the deformation resembles the geometry of the crystal field, in our example the two positive charges produce an ellipsoidal (cigar) shape. The crystal field striction arises from the fact, that a thermally (or magnetic field induced) change of the $4f$ charge density shape changes the force between the $4f$ ion and the positive charges which produce the crystal field. A magnetostrictive strain of the crystal lattice results as indicated by

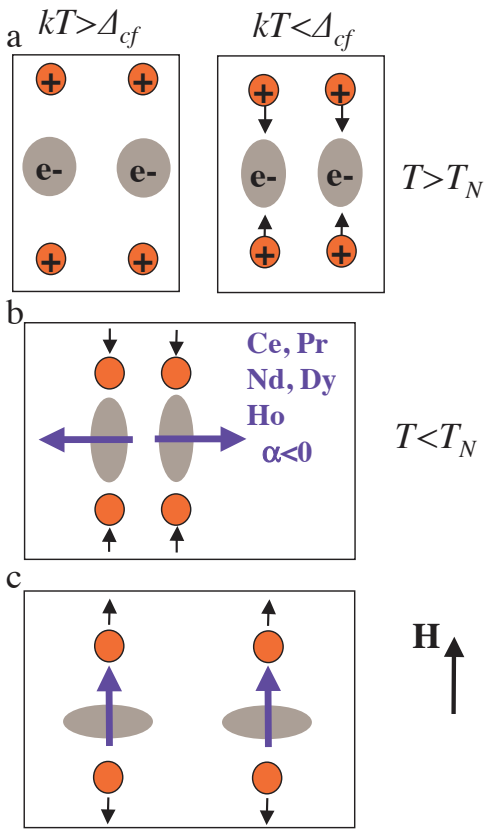

Figure 18: Crystal field (a-c) mechanism for magnetoelastic strains. For a description see text.

the small arrows in Fig. 18a-right. For this magnetostrictive effect no long range order is necessary and it is called crystal field influence on the thermal expansion [16, 17, 18].

We now consider what happens, when the system orders antiferromagnetically. The shape of the $4f$ charge density is closely associated with magnetic anisotropy. In crystal field theory this anisotropy is governed by Stevens factors α_j, β_j and γ_j [2] . In our simple example of Fig. 18a the magnetic easy axis will be vertical, i.e. along the revolution axis of the ellipsoid, if the sign of the Stevens factor α_j is *positive* (such as for Sm^{3+}, Er^{3+}, Tm^{3+}, Yb^{3+}). Conversly, if the sign of the Stevens factor α_j is *negative* (such as for Ce^{3+}, Pr^{3+}, Nd^{3+}, Tb^{3+}, Dy^{3+}, Ho^{3+}) the magnetic easy axis will be horizontal. We consider now rare earth with *negative* Stevens factors α_j: Below the Néel temperature T_N the magnetic moments order antiferromagnetically as indicated by the large arrows in Fig. 18b. The deformation of the $4f$ charge density already incipient above T_N is increased by the appereance of the magnetic moment and consequently leads to a spontaneous magnetostrictive effect below T_N as indicated by

the small arrows.

Due to the spin orbit coupling the orientation of the magnetic moment (easy axis) is coupled to the orientation of the $4f$ charge. The application of a magnetic field normal to the easy axis reduces the ellipsoidal deformation of the charge density and reverses the spontaneous magnetostrictive effect. If the magnetic field is strong enough, the charge density may even turn from an cigar shape into a pancake as shown in Fig. 18c. In a similar way the crystal field striction can be analysed for more complex configurations, where the shape of the charge density is more complicated.

Formally the crystal field striction can be described by considering the dependence of the crystal field parameters on the strain ϵ and the elastic energy $E_{\rm el}$:

$$\mathcal{H}_{\rm cf} = \sum_{lm,\mathbf{i}} B_l^m(\mathbf{i},\overline{\overline{\epsilon}}) O_l^m(\mathbf{J_i}) \tag{88}$$

$$E_{\rm el} = \frac{V}{2}\sum_{\alpha\beta} c_{\alpha\beta}\epsilon^\alpha\epsilon^\beta \tag{89}$$

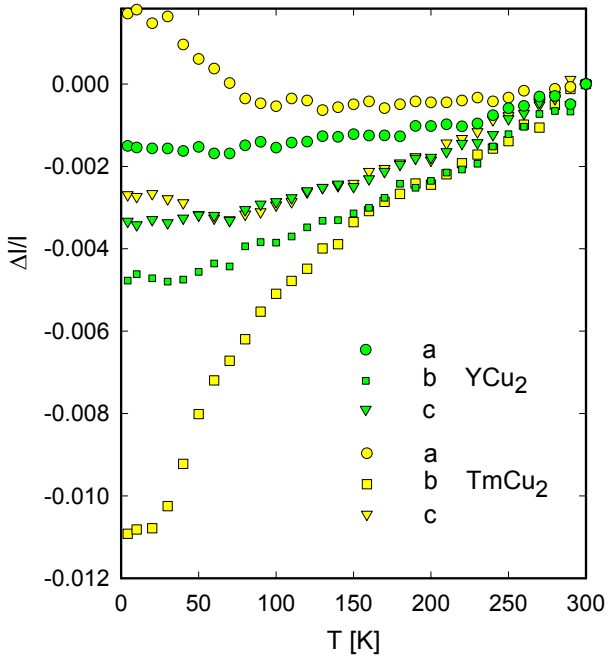

Figure 19: Lattice constants of $TmCu_2$ and nonmagnetic YCu_2 determined by temperature dependent powder x-ray diffraction and normalized to T=300 K.

If a magnetic field is applied, in addition the Zeman energy has to be considered:

$$\mathcal{H}_{\rm Ze} = -\sum_{\mathbf{i}} g_j \mu_B \boldsymbol{J}_{\mathbf{i}} \vec{B} \tag{90}$$

Starting point for the further analysis is the Taylor expansion of the crystal field parameters with respect to the components of the strain tensor $\overline{\overline{\epsilon}}$, leading to the so-called magnetoelastic Hamiltonian.

$$\sum_{lm,\mathbf{i}} B_l^m(\mathbf{i},\overline{\overline{\epsilon}})O_l^m(\mathbf{J_i}) \approx \sum_{lm,\mathbf{i}} B_l^m(\mathbf{i},\overline{\overline{\epsilon}}=0)O_l^m(\mathbf{J_i}) + \sum_{lm,\mathbf{i}} \epsilon^\alpha B_{l(\alpha)}^m(\mathbf{i})O_l^m(\mathbf{J_i}) + \cdots \tag{91}$$

with the magnetoelastic constants

$$B_{l(\alpha)}^m(\mathbf{i}) = \left[\frac{\partial B_l^m(\mathbf{i},\overline{\overline{\epsilon}})}{\partial \epsilon^\alpha}\right]_{\epsilon=0} \tag{92}$$

Usually the analysis is limited to the first order in the strain (harmonic approximation) and second order terms (anharmonic coupling) are neglected.

By definition the magnetic free energy is given by

$$F_m = -k_B T \ln Z \tag{93}$$

with the partition sum

$$Z = Tr\{e^{-\mathcal{H}/k_B T}\} \tag{94}$$

Here k_B denotes the Boltzmann constant. In our first order approach the trace in (94) is calculated using the states of the unperturbed system, i.e. without taking into account the magnetoelastic interactions, by putting $\overline{\overline{\epsilon}}=0$ in (88).

Inserting the Hamiltonian $\mathcal{H} = \mathcal{H}_{\rm cf} + E_{\rm el} + \mathcal{H}_{\rm Ze}$ (88) into (93) and (94), calculating the derivative of the magnetic free energy F_m with respect to the strains ϵ^α yields the final result

$$\epsilon_{cf}^\alpha = -\frac{1}{V}\sum_{\beta,\mathbf{i}} s^{\alpha\beta} B_{l(\alpha)}^m(\mathbf{i}) \langle O_l^m(\boldsymbol{J}_\mathbf{i})\rangle_{T,\vec{B}} \tag{95}$$

$$\tag{96}$$

Eqn. (95) shows that the complete temperature and field dependence of the strains can be calculated from thermal expectation values $\langle\rangle_{T,\vec{B}}$ of Stevens operator equivalents $\langle O_l^m(\boldsymbol{J}_\mathbf{i})\rangle_{T,\vec{B}}$. The magnetoelastic constants can either be derived from theoretical models [19] or, alternatively, enter as adjustable parameters into the theory. In principle some evidence can also be obtained from the shift of cef excitation spectra under pressure [20].

As an example for the crystal field striction effect we show the example $TmCu_2$ [17]. Note in the orthorhombic symmetry there are nine crystal field parameters to be considered: $B_2^0 = -0.94$ K, $B_2^2 = -1.23$ K, $B_4^0 = -0.9 \times 10^{-2}$ K, $B_4^2 = -0.39 \times 10^{-2}$ K,

$B_4^4 = -0.36 \times 10^{-2}$ K, $B_6^0 = 0.58 \times 10^{-4}$ K, $B_6^2 = 2.47 \times 10^{-4}$ K, $B_6^4 = -0.48 \times 10^{-4}$ K, $B_6^6 = 6.31 \times 10^{-4}$ K.

In order to determine the influence of the crystal field, the thermal expansion measured by temperature dependent powder x-ray diffraction is compared to the nonmagnetic isostructural system YCu_2. In Fig. 19 the lattice constants normalized to T=300 K are shown for both compounds.

The crystal field contribution to the thermal expansion can be determined by taking the difference of the strains and is shown in Fig. 20. It can be well described by the simple model equation

$$\epsilon_{cf}^{\alpha} = A_\alpha \langle O_2^0(\boldsymbol{J}) \rangle_T + B_\alpha \langle O_2^2(\boldsymbol{J}) \rangle_T \tag{97}$$

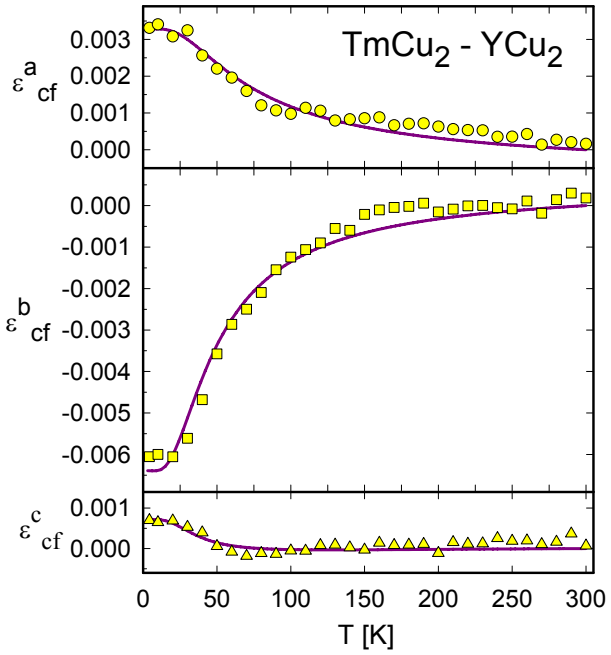

Figure 20: Difference of normalized lattice constants of $TmCu_2$ and YCu_2 versus temperature. The lines correspond to the results of the crystal field model for the thermal expansion.

with $A_1 = 5.9 \times 10^{-5}$, $A_2 = -1.1 \times 10^{-4}$, $A_3 = 1.1 \times 10^{-5}$, $B_1 = 2.1 \times 10^{-4}$, $B_2 = -3.9 \times 10^{-5}$, $B_3 = -6.6 \times 10^{-5}$.

4 Magnetic behaviour in complex metallic alloys: skutterudite $PrFe_4Sb_{12}$

Ternary skutterudites $RE_yTM_4X_{12}$ with RE = rare earth, TM = Fe, Co, Rh, Ru, ... and X = P, As, Sb, attracted much interest because of a variety of possible ground states and because of their large thermoelectric potential. Depending on the particular rare earth element, features like superconductivity as e.g., in $LaRu_4As_{12}$ below $T_c = 10.3$ K or $LaOs_4As_{12}$ below $T_c = 3.2$ K [21], long range magnetic order in $EuFe_4Sb_{12}$ at $T_{mag} = 84$ K [22, 23], heavy fermion behavior in $YbFe_4Sb_{12}$ [24], non-Fermi-liquid in $CeRu_4Sb_{12}$ [25], intermediate and mixed valence behavior in $Yb(Fe, Co)_4Sb_{12}$ and $Eu(Fe, Co)_4Sb_{12}$ [26, 27] and hopping conductivity in $YbRh_4Sb_{12}$ [26] were already found and discussed in some detail. Significant interest in this family of compounds, however, stems from the fact that skutterudites are potential candidates for thermoelectric applications. Materials considered for such a use should exhibit values for the *figure of merit* $ZT = S^2T/(\rho\lambda)$ at least of the order of one (T ... temperature, S ... Seebeck coefficient, ρ ... electrical resistivity and λ ... thermal conductivity). Depending on the carrier concentration of a particular skutterudite, Seebeck values above about 100 μV/K are frequently observed. Besides, ternary skutterudites are outstanding with respect to their low thermal conductivity which, in some cases, may be near to the theoretical limit. As a matter of fact, the dramatically diminished $\lambda(T)$ values are associated with an exceptionally large thermal displacement parameter of the loosely bound rare earth elements, corresponding to a "rattling" (i.e., soft phonon mode) of these atoms in an oversized cage [28].

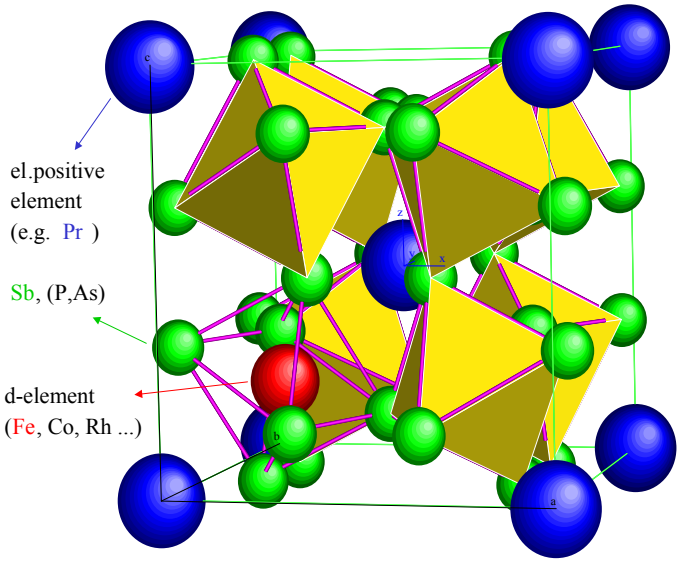

Figure 21: Crystal structure of $Pr_{0.73}Fe_4Sb_{12}$.

Specifically, $PrFe_4Sb_{12}$ is a cubic compound crystallizing in a body-centred cubic lattice; the local point symmetry of Pr is T_h (compare Fig. 21). As already mentioned, Pr is a non-Kramers ion. Then, the cubic symmetry is responsible for a splitting of the $j = 4$ total angular momentum of Pr^{3+} into a Γ_1 singlet, a Γ_3 doublet and in the Γ_4 and Γ_5 triplets. For non-Kramers ions like Pr, nonmagnetic ground states, i.e., Γ_1 and Γ_3, are possible.

Very recently, however, Takegahara et al. [29] have shown that the standard CEF Hamiltonian for simple cubic materials cannot be used for skutterudites, since systems with point groups T and T_h do not contain two types of symmetry of O_h, namely C_4, rotations through $\pi/2$ about the fourfold symmetry axis and C_2', Umklappung, rotations through π perpendicular to the principle rotation axis. Adding these symmetry properties reveals new six-order terms:

$$H^*_{cub} = B^0_4(O^0_4 + 5O^4_4) + B^0_6(O^0_6 - 21O^4_6) + B^2_6(O^2_6 - O^6_6) \tag{98}$$

where the previous notation is used. While, in general, the Hamiltonian Eqn. 98 leaves the degeneracy of the CEF states unchanged (in comparison to the standard CEF Hamiltonian for cubic symmetry), the wave functions, and thus matrix elements and magnetic moments are modified, depending on the magnitude of the additional six-order terms.

It is a good idea trying to obtain realistic CEF parameters B^m_l of a certain system from neutron inelastic scattering studies. Exposing at low temperatures a certain material to incoming neutrons within a so called triple-axis spectrometer or within a time-of-flight spectrometer, allows figure out excitations from the ground state CEF level to excited CEF levels. Such excitations are allowed only, if the matrix elements between two distinct states have finite values. Once, the temperature rises, the first, second, etc. level becomes thermally populated and new transitions between states are possible, i.e., other matrix elements show non-vanishing values. Note that such inelastic transitions may evolve in two different directions: neutrons may absorb energy from the system (at higher temperatures), or loose energy after a collision with the magnetic moment under consideration.

An evaluation of neutron inelastic scattering (NIS) data helps in general to define the CEF levels and their splitting from the ground state. Using least squares fitting, the CEF parameters B^m_l may be derived.

In the following subsection we will discuss the CEF scheme $PrFe_4Sb_{12}$ as derived from NIS studies at the time-of-flight instrument HET at ISIS, U.K., and will use the B^m_l data derived to describe a number of physical properties which are distinctly governed from CEF effects.

The magnetic parts of the inelastic neutron spectra S_M collected for $Pr_{0.73}Fe_4Sb_{12}$ at $T = 10$ K, $E_i = 11$ meV and $E_i = 40$ meV are shown in Figs. 22a,b. S_M is derived by comparison with the respective data of $LaFe_4Sb_{12}$ [30]. The low energy excitations are decomposed into a quasielastic line and an inelastic line centred at $E_1 = 2.2$ meV. The

spectrum at higher incident energy reveals additional inelastic lines at $E_2 = 10.7$ meV and $E_3 = 16.8$ meV.

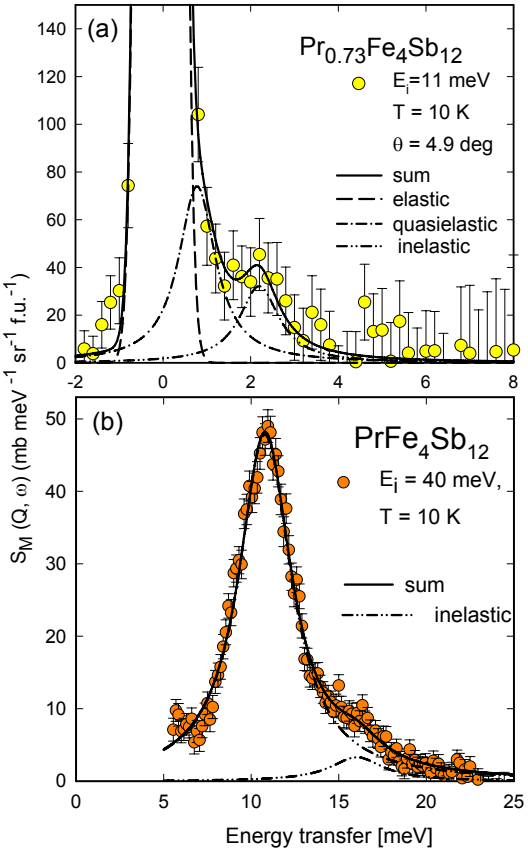

Figure 22: Energy dependent magnetic scattering intensity S_M of $Pr_{0.73}Fe_4Sb_{12}$. (a): $T = 10$ K, $E_i = 11$ meV; (b): $T = 10$ K, $E_i = 40$ meV. The solid, dashed, dashed-dot and dashed-dot-dot lines describe the sum, elastic, quasielastic, and inelastic contributions, respectively.

Considering the experimentally observed values of inelastic CEF excitations in the context of Eqn. 98, a set of CEF parameters is obtained: $B_4^0 = 0.03712$ K, $B_6^0 = 0.00125$ K and $B_6^2 = 0.001$ K, matching the estimated parameters $B_4^0 = 0.04$ K and $B_6^0 = 0.00133$ K derived, when only a simple cubic Hamiltonian is considered [31]. These values determine the wave functions of the various eigenstates and cause the triplet $\Gamma_4^{(2)}$ to be the ground state of the system. $\Gamma_4^{(2)}$, which in the simple version of the Hamiltonian corresponds to the triplet Γ_5, possesses a magnetic moment and thus can give rise to an ordered ground state. In fact, various bulk properties of $Pr_{0.73}Fe_4Sb_{12}$ indicate ordering below about 4.6 K [31, 32]. The singlet Γ_1 is situated 25.8 K above the ground state. Additionally, the strong quasielastic peak (compare Fig. 22) would

favour a triplet state, while an absence of this contribution would be in line with a singlet ground state.

Differences between the appropriate Hamiltonian for skutterudites (Eqn. 98) and the standard Hamiltonian for cubic systems (comapre e.g. Eqn. 37) are small e.g., for thermodynamic quantities like the specific heat, but have severe consequences for properties like the neutron inelastic scattering, where the intensity of a distinct transition depends on the square of the appropriate matrix element, i.e. $|\langle\Gamma_i|J_z|\Gamma_j\rangle|^2$, where Γ_i and Γ_j represent the initial and the final CEF state, respectively. If this matrix element vanishes, a transition will likely not occur, and no neutron inelastic scattering intensity (in general a Lorentzian line) will be found centered at an energy $\Delta = \Delta(\Gamma_j) - \Delta(\Gamma_i)$.

The fact that a singlet state Γ_1 is observed roughly 25 K above the magnetic ground state triplet in $Pr_{0.73}Fe_4Sb_{12}$ would not be accounted for by the Hamiltonian Eqn. 37, where $|\langle\Gamma_5|J_z|\Gamma_1\rangle|^2 = 0$. Within the dipole selection rules, the eigenstates of both CEF level are not bridged by $m_j = \pm 1$. On the contrary, taking into account the Hamiltonian for Skutterudites, Eqn. 98, a finite matrix element is found, i.e., $|\langle\Gamma_4^2|J_z|\Gamma_1\rangle|^2 \neq 0$, thus intensity may be observed, as it is obvious from Fig. 22. Differences regarding the resulting CEF schemes of both CEF Hamiltonians applied to $Pr_{0.73}Fe_4Sb_{12}$ are sketched in Fig. 23.

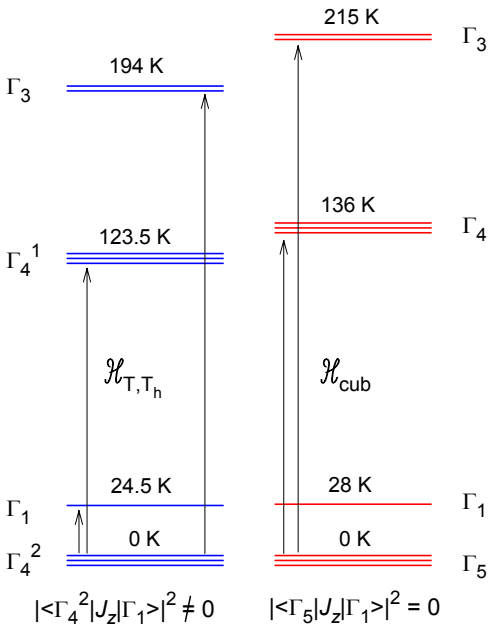

Figure 23: CEF scheme of $Pr_{0.73}Fe_4Sb_{12}$ derived from both Hamiltonians Eqn. 98 (left) and Eqn. 37 (right).

Results of magnetic susceptibility measurements performed on $Pr_{0.73}Fe_4Sb_{12}$ are shown in Figs. 24 (a,b). The Curie-Weiss like behavior at elevated temperatures ($T >$

50 K) reveals an effective magnetic moment $\mu_{\rm eff} = 4.19\ \mu_{\rm B}$, as well as a paramagnetic Curie temperature $\theta_p \approx 0.5$ K. In order to match the theoretical rare earth moments associated with a 3+ state of the Pr ion, a significant contribution to μ_{eff} of the $[Fe_4Sb_{12}]$ sublattice is required. Assuming that both the rare earth and the $[Fe_4Sb_{12}]$ contribution to μ_{eff} are simply additive, i.e.,

$$\mu_{eff}^{meas.} = \sqrt{y\left(\mu_{eff}^{Pr}\right)^2 + \left(\mu_{eff}^{[Fe_4Sb_{12}]}\right)^2} \tag{99}$$

(y is the void filling factor) yields an effective magnetic moment for $[Fe_4Sb_{12}]$ of 2.7 $\mu_{\rm B}$.

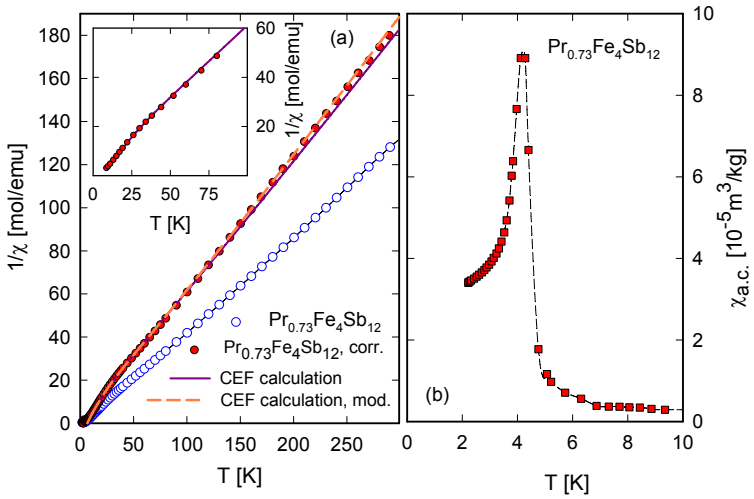

Figure 24: (a): Temperature dependent magnetic susceptibility χ of $Pr_{0.73}Fe_4Sb_{12}$ and $Nd_{0.72}Fe_4Sb_{12}$ plotted as χ^{-1} vs. T. The solid circles represent the Pr-related susceptibility and the solid line is a least squares fit according to Eqn. 2. The inset shows the low temperature behavior in more detail. (b): $\chi_{a.c.}(T)$ of $Pr_{0.73}Fe_4Sb_{12}$ and $Nd_{0.72}Fe_4Sb_{12}$.

A closer inspection of the low temperature data and of the a.c. measurement (Fig. 24(b)) indicates an onset of long range magnetic order. Defining the transition temperature of $Pr_{0.73}Fe_4Sb_{12}$ in a standard manner, i.e., by taking the extremum in $\mathrm{d}\chi_{dc}T/\mathrm{d}T$ as well as the temperature at half height of the a.c. susceptibility anomaly on the paramagnetic side reveals $T_{mag} \approx 4.6$ K. The sharp transition and the overall behavior of $\chi_{a.c.}(T)$ does not exclude a ferromagnetic ground state.

To fix the contribution originated by Pr, the susceptibility associated with $[Fe_4Sb_{12}]$ is subtracted from the total measured set of data assuming a simple Curie behavior and taking into account $\mu_{eff}([Fe_4Sb_{12}]) = 2.7\mu_B$. The thus modified $1/\chi(T)$ curve is added in Fig. 24 (a).

The susceptibility $\chi(T)$ related to Pr in $Pr_{0.73}Fe_4Sb_{12}$ is analyzed in terms of

$$1/\chi = 1/\chi_{CEF} - \lambda \tag{100}$$

where χ_{CEF} is the susceptibility due to crystal field effects and λ is the molecular field parameter caused by exchange interactions between the Pr ions. Note a substantially large value of λ originates a magnetic instability of a certain system.

Taking into account the CEF parameters B_l^m derived from the NIS study, in the context of Eqn. 83 allows the calculation of $\chi_{CEF}(T)$ as well as of $\chi(T)$ by adjusting λ. A reasonable fit of the experimental data is obtained for $\lambda = 6$ mol/emu. Results of the calculation are shown in Fig. 24(a) as solid line. In particular, the pronounced curvature in $1/\chi(T)$ around 25 K is well reproduced (compare inset, Fig. 24 (a)) and the overall susceptibility behaviour matches fairly well the experiment.

Associated with the Γ_4^2 triplet ground state is a magnetic moment of $\mu = 2\ \mu_B$. This finding is consistent with the occurrence of magnetic order and moreover explains the magnitude of the isothermal magnetization at $T = 2$ K.

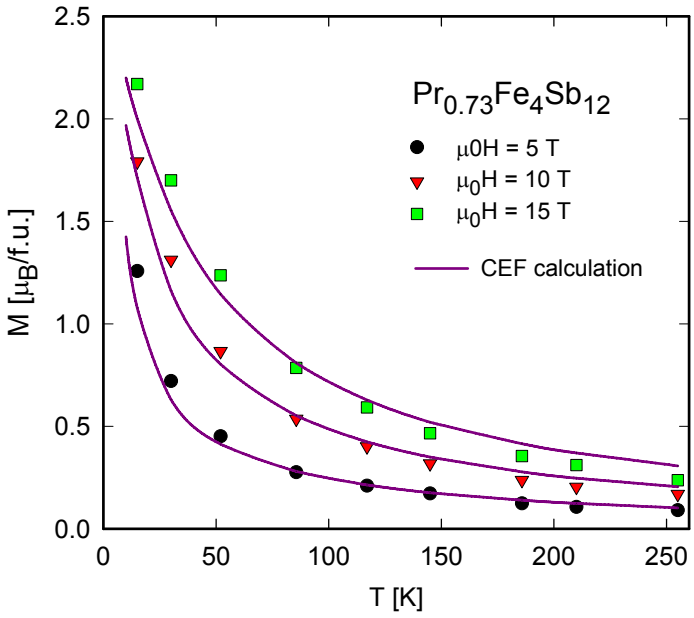

Figure 25: Temperature dependent magnetization of $Pr_{0.73}Fe_4Sb_{12}$ for various values of externally applied magnetic fields. The solid lines are theoretical values (see text).

Magnetization measurements performed up to 15 T are an additional possibility to consider crystal field effects and to corroborate the set of the CEF parameters chosen. Plotted in Fig. 25 is the temperature dependent magnetization for various values of applied magnetic fields. The solid lines are calculations of the magnetization based on Eqn. 98 with $g_j = 4/5$, $j = 4$, and the above indicated CEF parameters, revealing reasonable agreement with the experimental data. Note, there is no extra adjustable parameter used in this calculation.

Shown in Fig. 26is the temperature dependent electrical resistivity $\rho(T)$ of

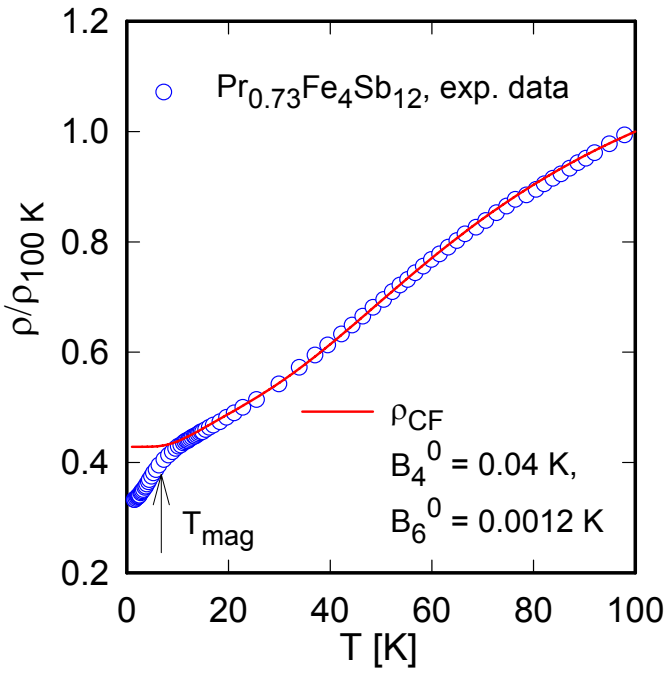

Figure 26: Normalized resistivity of $Pr_{0.73}Fe_4Sb_{12}$. The solid line represents the CEF derived spindisorder resistivity as derived from the CEF parameters of $Pr_{0.73}Fe_4Sb_{12}$.

$Pr_{0.73}Fe_4Sb_{12}$. The compound behave metallic, i.e., $\rho(T)$ increases with rising temperature. The particular temperature dependence, however, deviates significantly from a simple metal and is characteristic for materials having a reduced number of charge carriers. At low temperatures, the weak anomaly in $Pr_{0.73}Fe_4Sb_{12}$ indicates the onset of long range magnetic order at 4.6 K.

To account for the strongly curved $\rho(T)$ behavior of $Pr_{0.73}Fe_4Sb_{12}$, at least in the lower temperature range ($T < 100$ K), the spin disorder resistivity ρ_{spd} is considered, i.e., scattering of conduction electrons on disordered magnetic moments, in combination with CEF effects, compare Eqn. 87.

Using the already derived CEF parameters the normalized spin disorder contribution to the electrical resistivity can be calculated without any further free parameters. Results of this calculation are shown in Fig. 26, together with the resistivity data of $Pr_{0.73}Fe_4Sb_{12}$ normalized to 100 K. Except at low temperatures, where $Pr_{0.73}Fe_4Sb_{12}$ exhibits a phase transition ($T_{mag} = 4.6$ K), the peculiar structure of $\rho(T)$ is well reproduced by this choice of CEF parameters.

5 Summary and Outlook

Subjects which could not be touched in this chapter should be briefly mentioned. There is on one hand the extension of the theory to include higher multiplets, such as necessary for example in the case of Sm and Eu [33]. Moreover, in some peculiar cases the crystal field may be influenced significantly by optical phonons propagating through the crystal. Such a situation is described by a large crystal field phonon interaction [34], which produces usually a strong damping and consequently increased linewidth of the crystal field excitations spectra. Similar, there may be a strong coupling to the conduction electrons resulting also in increased linewidth effects [35]. Moreover, such couplings may result in a temperature dependence of the crystal field excitation energies [36]. In very special cases a strong crystal field phonon coupling may lead to bound states, which have partly crystal field and partly phonon character with a characteristic anticrossing in the dispersion relation [37].

If the crystal field ground state is degenerate it may couple strongly to some lattice strain and below a characteristic temperature the system may lower its lattice symmetry thus lifting the degeneracy of the cf ground state. Such a Jahn Teller effect is often observed, when there are no significant two ion interactions present [38]. However, in most rare earth systems, two ion interactions are dominant and lead to long range order. The two ion interactions in the simplest case are isotropic and bilinear, such as for instance the direct (Heisenberg) exchange interaction and the indirect exchange interactions (RKKY, superexchange etc.). In many cases there is strong evidence for anisotropic bilinear interactions [39], such as the classical dipolar interaction, anisotropic exchange or the completely antisymmetric Dzyaloshinski-Moriya interaction. In many cases the bilinear interactions scale with the de'Gennes factor. When this factor is small, as for example in the case of Pr and Tm, other types of two ion interactions may become dominant, such as for example the quadrupolar interactions [38]. The Jahn Teller effect in this view is driven by such an effective quadrupolar interaction. However, there exist also "true" two ion quadrupolar or orbital interactions, which are not coupled to a strong lattice distortion. The static behavior of the ordered states can be extremely complex and is usually treated in mean field theory [40].

Any two ion interaction will influence not only the static behavior of the system, but also modify the excitation spectrum. If only the crystal field interaction is present, the magnetic modes do not show any dispersion and the main effect of two ion interactions is to produce dispersion in the magnetic excitations. This dispersion can be calculated from the Fourier transform of the two ion interactions within the random phase approximation [40, 41]. If the crystal field interaction is weak compared to the bilinear (quadrupolar, orbital) interaction the corresponding dispersive excitations are usually called magnons (orbitons).

For a quantitative analysis of the crystal field, software programs have been developed. The most popular program is probably *cfield*, which is a part of the *McPhase*

package [42] [3]. *McPhase* is a modeling suite for complex problems in magnetism, which allows the quantitative evaluation of most of the effects described above, i.e. long range order, dispersion of excitations [39] etc. As a result of such a modeling exchange and crystal field parameters can be quantitatively determined. Moreover, by a quantitative analysis in some cases clear discrepancies between the predictions of the standard model of rare earth magnetism and the experimental data have been identified. As examples we mention (i) the discovery of additional excitations in $CeCu_2$, which are not allowed by symmetry [43]; (ii) the discovery of the magnetoelastic paradox in Gd based compounds [44, 45]. These examples demonstrate, that the numerical evaluation of models in magnetism allows to confront theoretical concepts with experimental observations. Discrepancies between experiment and theory, wich become evident in this way will help to improve our understanding of magnetism.

Computing programs for multiplet mixing and optical spectra

SPECTRA - for optical CEF spectra http://chemistry.anl.gov/downloads/spectra/ 1. B.Z. Malkin, in Spectroscopy of Solids Containing Rare Earth Ions, Ed. By A. A. Kaplyanskii and R. M. MacFarlane, Ch.2, 13 (North-Holland, Amsterdam, 1987). 2. W. T. Carnall, J. Chem. Phys., 96, 8713 (1992). 3. B. R. Judd, Phys. Rev. 141, 4-14 (1966). 4. H. Crosswhite, H. M. Crosswhite and B. R. Judd, Phys. Rev. 174, 89-94 (1968). 5. H. H. Marvin, Phys. Rev. 71, 102 (1947). 6. B. R. Judd, H. M. Crosswhite, and H. Crosswhite, Phys. Rev. 169, 130 (1967). 7. R. Storn and K. Price, J. Global Optimization, 11, 341(1997).

Recommended Textbooks

1. R. D. Cowan, The Theory of Atomic Structure and Spectra (University of California Press, Berkeley, 1981). 2. C. W. Nielson and G. F. Koster, Spectroscopic Coefficients for the pn, dn, and fn Configurations (MIT Press, Cambridge, 1963). 3. B. G. Wybourne, Spectroscopic Properties of Rare Earths (Interscience, New York, 1965). 4. I. Sobelman, Atomic Spectra and Radiative Transitions (Springer, Berlin, 1992), 2nd ed. 5. S.Hufner, Optical Spectra of Transparent Rare Earth Compounds (Academic Press, 1978). 6. B.R. Judd, Operator Techniques in Atomic Spectroscopy (Princeton University Press, 1998).

References

[1] see e.g., J. Crangle, *Solid State Magnetism*, (Edward Arnold, London 1991).

[2] M. T. Hutchings, in: *Solid State Physics* Vol. 16, ed. F. Seitz and D. Thurnbull, Academic Press, New York and London (1964) 227.

[3] www.mcphase.de

[3] P. Fulde, in *Handbook on the Physics and Chemistry of Rare Earths*, ch. 17 p. 295 ed. K. A. Gschneidner and L. Eyring, North Holland Publishing Company 1978.

[4] P. Fulde and M. Loewenhaupt, *Adv. Physics* **34** (1985) 589.

[5] A.J. Freeman and R.E. Watson, Phys. Rev. **127** (1962) 2058.

[6] W. B. Lewis and J. B. Mann and D. A. Liberman and D. T. Cromer, J. of Chem. Phys., **53** (1970) 809.

[7] K. W. H. Stevens, *Proc. Phys. Soc.* **A 65** (1952) 209.

[8] A.J. Freeman, *Magnetic Properties of Rare Earth Metals*, ed. by R.J. Elliot (Plenum, New York, 1972.

[9] C. Cohen-Tannoudji, Claude, *Quantum Mechanics*, Wiley John + Sons, 1977 ISBN: 047116433X.

[10] U. Walter, *Phys. Rev.* **B 36** (1987) 2504.

[11] J. Sereni, in *Handbook on the Physics and Chemistry of Rare Earths*, ch. 98 p. 295 ed. K. A. Gschneidner and L. Eyring, (Elsevier Science Publishers B.V., Amsterdam, 1978).

[12] T. Murao and T. Matsubara, Prog. Theor. Phys. **18**, 215 (1957).

[13] V.U.S. Rao and W.E. Wallace, Phys. Rev. B **2**, 4613 (1970).

[14] P. Fulde and M. Loewenhaupt, *Adv. in Physics* **34** (1986) 589.

[15] M. Doerr, M. Rotter and A. Lindbaum, *Adv. Phys.* **54** (2005) 1.

[16] E. Gratz, M. Rotter, A. Lindbaum, H. Müller, E. Bauer and H. Kirchmayr, *J. Phys. Cond. Mat.* **5** (1993) 567.

[17] E. Gratz, A. Lindbaum and M. Rotter, *J. Phys. Cond. Mat.* **5** (1993) 7955.

[18] E. Gratz, M. Rotter, A. Lindbaum, H. Müller, E. Bauer and H. Kirchmayr, *Materials Science Forum* **133-136** (1993) 461.

[19] K. Hense, PhD thesis Technische Universität Wien (2002).

[20] M. Rotter, M. Doerr, M. Loewenhaupt, W. Kockelmann, R. I. Bewley, R. S. Eccleston, A. Schneidewind and G. Behr, *J. Magn. Magn. Mat.* **269** (2004) 372.

[21] I. Shirotani, K. Ohno, C. Sekine, T. Yagi, T. Kawakami, T. Nakanishi, H. Takahashi, J. Tang, A. Matsushita, and T. Matsumoto, Physica B **281-282** (2000) 1021.

[22] M.E. Danebrock, C.B.H. Evers, and W. Jeitschko, J. Phys. Chem. Solids, **57** (1996) 381.

[23] E. Bauer, St. Berger, A. Galatanu, M. Galli, H. Michor, G. Hilscher, Ch. Paul, B. Ni, M.M. Abd-Elmeguid, V.H. Tran, A. Grytsiv, and P. Rogl, Phys. Rev. B **63** (2001) 224414.

[24] N.R. Dilley, E.J. Freeman, E.D. Bauer, and M.B. Maple, Phys. Rev. B **58** (1998) 6287.

[25] N. Takeda and M. Ishikawa, J.Phys.: Cond. Mat. **13** (2001) 5971.

[26] E. Bauer, A. Galatanu, H. Michor, G. Hilscher, P. Rogl, P. Boulet, and H. Noël, Eur. Phys. J. B **14** (2000) 483.

[27] A. Grytsiv, P. Rogl, St. Berger, Ch. Paul, E. Bauer, C. Godart, B. Ni, M.M. Abd-Elmeguid, A. Saccone, R. Ferro, and D. Kaczorowski, Phys. Rev. B **66** (2002) 094411.

[28] G.S. Nolas, D.T. Morelli, and T.M. Tritt, Annu. Rev. Mater. Sci **29** (1999) 89 , and references therein.

[29] K. Takegahara and H. Harima, J. Phys. Soc. Japan J. Phys. Soc. Jpn. **70** (2001) 1190.

[30] D. T. Adroja, J.-G. Park, K. A. McEwen, N. Takeda, M. Ishikawa and J.-Y. So Phys. Rev. B **68** (2003) 094425.

[31] E. Bauer, St. Berger, Ch. Paul, M. Della Mea, G. Hilscher, H. Michor, M. Reissner, W. Steiner A. Grytsiv, P. Rogl and E. W. Scheidt, Phys. Rev. B **66** (2002) 214421.

[32] N. P. Butch, W. M. Yuhasz, P.-C. Ho, J. R. Jeffries, N. A. Frederick, T. A. Sayles, X. G. Zheng, M. B. Maple, F. M. Woodward, J. W. Lynn, P. Rogl and G. Giester Phys. Rev. B **71** (2005) 214417.

[33] M. Loewenhaupt, Physica B **130** (1985) 347.

[34] M. Loewenhaupt and U. Witte, *J. Phys.: Cond. Mat.* **15** (2003) S519.

[35] K.W. Becker, P. Fulde and J. Keller, Z. Phys. B **28** (1977) 9.

[36] K. Hense, U. Witte, M. Rotter, R. Schedler, E. Gratz, H. Nowotny and M. Loewenhaupt, *J. Magn. Mag. Mat.* **272-276** (2004) 387.

[37] P. Thalmeier and P. Fulde, Phys. Rev. Lett. **49** (1982) 1588.

[38] P. Morin and D. Schmitt, in: *Ferromagnetic Materials* Vol. 5, ed. K. H. J. Buschow and E. P. Wohlfarth, Elsevier Sci. Pub. Amsterdam,The Netherlands (1990) 1.

[39] M. Rotter, M. Loewenhaupt, S. Kramp, T. Reif, N. M. Pyka, W. Schmidt and R. v. d. Kamp, *Europ. Phys. J.* **B 14** (2000) 29.

[40] J. Jensen and A. R. Mackintosh, *Rare Earth Magnetism*, Clarendon Press, Oxford, (1991).

[41] M. Rotter J. of Comp. Mat. Sci. **38** (2006) 404.

[42] M. Rotter, *J. Magn. Mag. Mat.* **272-276** (2004) e481.

[43] M. Loewenhaupt, R. Schedler, U. Witte, M. Rotter and W. Schmidt, Physica B **378-380** (2006), 775.

[44] M. Rotter, A. Lindbaum, M. Doerr, M. Loewenhaupt, A. Barcza, M. el Massalami and B. Beuneu, *Europhys. Lett.* **75** (2006) 160.

[45] M. Rotter, M. Doerr, M. Zschintzsch, A. Lindbaum, H. Sassik and G. Behr, J. Magn. Magn. Mat., **310**, (2007) 1383.

A Stevens Operators

The appendix summarises all Stevens operators and the tesseral harmonics.
$X = J(J+1)$

$$
\begin{aligned}
O_0^0 &= 1 \\
\hline
O_1^{-1} &= \frac{-i}{2}[J_+ - J_-] = J_y \\
O_1^0 &= J_z \\
O_1^1 &= \frac{1}{2}[J_+ + J_-] = J_x \\
\hline
O_2^{-2} &= \frac{-i}{2}[J_+^2 - J_-^2] = J_xJ_y + J_yJ_x = 2P_{xy} \\
O_2^{-1} &= \frac{-i}{4}[J_z(J_+ - J_-) + (J_+ - J_-)J_z] = \frac{1}{2}[J_yJ_z + J_zJ_y] = P_{yz} \\
O_2^0 &= [3J_z^2 - X] \\
O_2^1 &= \frac{1}{4}[J_z(J_+ + J_-) + (J_+ + J_-)J_z] = \frac{1}{2}[J_xJ_z + J_zJ_x] = P_{xz} \\
O_2^2 &= \frac{1}{2}[J_+^2 + J_-^2] = J_x^2 - J_y^2 \\
\hline
O_3^{-3} &= \frac{-i}{2}[J_+^3 - J_-^3]
\end{aligned}
$$

$$
\begin{aligned}
O_3^{-2} &= \frac{-i}{4}[(J_+^2 - J_-^2)J_z + J_z(J_+^2 - J_-^2)] \\
O_3^{-1} &= \frac{-i}{4}[(J_+ - J_-)(5J_z^2 - X - 1/2) + (J_+ - J_-)(5J_z^2 - X - 1/2)(J_+ - J_-)] \\
O_3^{0} &= [5J_z^3 - (3X-1)J_z] \\
O_3^{1} &= \frac{1}{4}[(J_+ + J_-)(10J_z^2 - 2X - 1) + (5J_z^2 - X - 1/2)(J_+ + J_-)] \\
O_3^{2} &= \frac{1}{4}[(J_+^2 + J_-^2)J_z + J_z(J_+^2 + J_-^2)] \\
O_3^{3} &= \frac{1}{2}[J_+^3 + J_-^3] \\
\hline
O_4^{-4} &= \frac{-i}{2}[(J_+^4 - J_-^4] \\
O_4^{-3} &= \frac{-i}{4}[(J_+^3 - J_-^3)J_z + J_z(J_+^3 - J_-^3)] \\
O_4^{-2} &= \frac{-i}{4}[(J_+^2 - J_-^2)(7J_z^2 - X - 5) + (7J_z^2 - X - 5)(J_+^2 - J_-^2)] \\
O_4^{-1} &= \frac{-i}{4}[(J_+ - J_-)(7J_z^3 - (3X+1)J_z) + (7J_z^3 - (3X+1)J_z)(J_+ - J_-)] \\
O_4^{0} &= [35J_z^4 - (30X - 25)J_z^2 + 3X^2 - 6X] \\
O_4^{1} &= \frac{1}{4}[(J_+ + J_-)(7J_z^3 - (3X+1)J_z) + (7J_z^3 - (3X+1)J_z)(J_+ + J_-)] \\
O_4^{2} &= \frac{1}{4}[(J_+^2 + J_-^2)(7J_z^2 - X - 5) + (7J_z^2 - X - 5)(J_+^2 + J_-^2)] \\
O_4^{3} &= \frac{1}{4}[(J_+^3 + J_-^3)J_z + J_z(J_+^3 + J_-^3)] \\
O_4^{4} &= \frac{1}{2}[(J_+^4 + J_-^4] \\
\hline
O_5^{-5} &= \frac{-i}{2}[J_+^5 - J_-^5] \\
O_5^{-4} &= \frac{-i}{4}[(J_+^4 - J_-^4)J_z + J_z(J_+^4 - J_-^4)] \\
O_5^{-3} &= \frac{-i}{4}[(J_+^3 - J_-^3)(9J_z^2 - X - 33/2) + (9J_z^2 - X - 33/2)(J_+^3 - J_-^3)] \\
O_5^{-2} &= \frac{-i}{4}[(J_+^2 - J_-^2)(3J_z^3 - (X+6)J_z) + (3J_z^3 - (X+6)J_z)(J_+^2 - J_-^2)] \\
O_5^{-1} &= \frac{-i}{4}[(J_+ - J_-)\{21J_z^4 - 14J_z^2X + X^2 - X + 3/2\} + \{\ldots\}(J_+ - J_-)] \\
O_5^{0} &= [63J_z^5 - (70X - 105)J_z^3 + (15X^2 - 50X + 12)J_z] \\
O_5^{1} &= \frac{1}{4}[(J_+ + J_-)(21J_z^4 - 14J_z^2X + X^2 - X + 3/2) + \\
&+ (21J_z^4 - 14J_z^2X + X^2 - X + 3/2)(J_+ + J_-)]
\end{aligned}
$$

$$
\begin{aligned}
O_5^2 &= \frac{1}{4}[(J_+^2+J_-^2)(3J_z^3-(X+6)J_z)+(3J_z^3-(X+6)J_z)(J_+^2+J_-^2)] \\
O_5^3 &= \frac{1}{4}[(J_+^3+J_-^3)(9J_z^2-X-33/2)+(9J_z^2-X-33/2)(J_+^3+J_-^3)] \\
O_5^4 &= \frac{1}{4}[(J_+^4+J_-^4)J_z+J_z(J_+^4+J_-^4)] \\
O_5^5 &= \frac{1}{2}[J_+^5+J_-^5] \\
\hline
O_6^{-6} &= \frac{-i}{2}[J_+^6-J_-^6] \\
O_6^{-5} &= \frac{-i}{4}[(J_+^5-J_-^5)J_z+J_z(J_+^5-J_-^5)] \\
O_6^{-4} &= \frac{-i}{4}[(J_+^4-J_-^4)(11J_z^2-X-38)+(11J_z^2-X-38)(J_+^4-J_-^4)] \\
O_6^{-3} &= \frac{-i}{4}[(J_+^3-J_-^3)(11J_z^3-(3X+59)J_z)+(J_+^3+J_-^3)(11J_z^3-(3X+59)J_z)(J_+^3-J_-^3)] \\
O_6^{-2} &= \frac{-i}{4}[(J_+^2-J_-^2)\{33J_z^4-(18X+123)J_z^2+X^2+10X+102\}+\{\ldots\}(J_+^2-J_-^2)] \\
O_6^{-1} &= \frac{-i}{4}[(J_+-J_-)\{33J_z^5-(30X-15)J_z^3+(5X^2-10X+12)J_z\}+\{\ldots\}(J_+-J_-)] \\
O_6^0 &= [231J_z^6-(315X-735)J_z^4+(105X^2-525X+294)J_z^2-5X^3+40X^2-60X] \\
O_6^1 &= \frac{1}{4}[(J_++J_-)\{33J_z^5-(30X-15)J_z^3+(5X^2-10X+12)J_z\}+\{\ldots\}(J_++J_-)] \\
O_6^2 &= \frac{1}{4}[(J_+^2+J_-^2)\{33J_z^4-(18X+123)J_z^2+X^2+10X+102\}+\{\ldots\}(J_+^2+J_-^2)] \\
O_6^3 &= \frac{1}{4}[(J_+^3+J_-^3)(11J_z^3-(3X+59)J_z)+(J_+^3+J_-^3)(11J_z^3-(3X+59)J_z)(J_+^3+J_-^3)] \\
O_6^4 &= \frac{1}{4}[(J_+^4+J_-^4)(11J_z^2-X-38)+(11J_z^2-X-38)(J_+^4+J_-^4)] \\
O_6^5 &= \frac{1}{4}[(J_+^5+J_-^5)J_z+J_z(J_+^5+J_-^5)] \\
O_6^6 &= \frac{1}{2}[J_+^6+J_-^6]
\end{aligned}
$$

B Tesseral Harmonics

$$
\begin{aligned}
Z_0^0 &= \frac{1}{\sqrt{4\pi}} \\
\hline
Z_1^{-1} &= \sqrt{\frac{3}{4\pi}}[y/r]
\end{aligned}
$$

$$
\begin{aligned}
Z_1^0 &= \sqrt{\frac{3}{4\pi}}[z/r] \\
Z_1^{+1} &= \sqrt{\frac{3}{4\pi}}[x/r] \\
\hline
Z_2^{-2} &= \frac{1}{4}\sqrt{\frac{15}{\pi}}[2xy/r^2] \\
Z_2^{-1} &= \frac{1}{2}\sqrt{\frac{15}{\pi}}[yz/r^2] \\
Z_2^0 &= \frac{1}{4}\sqrt{\frac{5}{\pi}}[(3z^2-r^2)/r^2] \\
Z_2^{+1} &= \frac{1}{2}\sqrt{\frac{15}{\pi}}[xz/r^2] \\
Z_2^{+2} &= \frac{1}{4}\sqrt{\frac{15}{\pi}}[(x^2-y^2)/r^2] \\
\hline
Z_3^{-3} &= \sqrt{\frac{35}{32\pi}}[(3x^2y-y^3)/r^3] \\
Z_3^{-2} &= \sqrt{\frac{105}{16\pi}}[2xyz/r^3] \\
Z_3^{-1} &= \sqrt{\frac{21}{32\pi}}[y(5z^2-r^2)/r^3] \\
Z_3^0 &= \sqrt{\frac{7}{16\pi}}[z(5z^2-3r^2)/r^3] \\
Z_3^{+1} &= \sqrt{\frac{21}{32\pi}}[x(5z^2-r^2)/r^3] \\
Z_3^{+2} &= \sqrt{\frac{105}{16\pi}}[(x^2-y^2)z/r^3] \\
Z_3^{+3} &= \sqrt{\frac{35}{32\pi}}[(x^3-3xy^2)/r^3] \\
\hline
Z_4^{-4} &= \frac{3}{16}\sqrt{\frac{35}{\pi}}[4(x^3y-xy^3)/r^4] \\
Z_4^{-3} &= \frac{3}{8}\sqrt{\frac{70}{\pi}}[(3x^2y-y^3)z/r^4] \\
Z_4^{-2} &= \frac{3}{8}\sqrt{\frac{5}{\pi}}[2xy(7z^2-r^2)/r^4] \\
Z_4^{-1} &= \frac{3}{4}\sqrt{\frac{5}{2\pi}}[yz(7z^2-3r^2)/r^4]
\end{aligned}
$$

$$
\begin{aligned}
Z_4^0 &= \frac{3}{16}\frac{1}{\sqrt{\pi}}[35z^4 - 30z^2r^2 + 3r^4)/r^4] \\
Z_4^{+1} &= \frac{3}{4}\sqrt{\frac{5}{2\pi}}[xz(7z^2 - 3r^2)/r^4] \\
Z_4^{+2} &= \frac{3}{8}\sqrt{\frac{5}{\pi}}[(x^2 - y^2)(7z^2 - r^2)/r^4] \\
Z_4^{+3} &= \frac{3}{8}\sqrt{\frac{70}{\pi}}[(x^3 - 3xy^2)z/r^4] \\
Z_4^{+4} &= \frac{3}{16}\sqrt{\frac{35}{\pi}}[(x^4 - 6x^2y^2 + y^4)/r^4] \\
\hline
Z_5^{-5} &= \sqrt{\frac{693}{512\pi}}[(5x^4y - 10x^2y^3 + y^5)/r^5] \\
Z_5^{-4} &= \sqrt{\frac{3465}{256\pi}}[4(x^3y - xy^3)z/r^5] \\
Z_5^{-3} &= \sqrt{\frac{385}{512\pi}}[(3x^2y - y^3)(9z^2 - r^2)/r^5] \\
Z_5^{-2} &= \sqrt{\frac{1155}{64\pi}}[2xy(3z^3 - zr^2)/r^5] \\
Z_5^{-1} &= \sqrt{\frac{165}{256\pi}}[y(21z^4 - 14z^2r^2 + r^4)/r^5] \\
Z_5^0 &= \sqrt{\frac{11}{256\pi}}[(63z^5 - 70z^3r^2 + 15zr^4)/r^5] \\
Z_5^{+1} &= \sqrt{\frac{165}{256\pi}}[x(21z^4 - 14z^2r^2 + r^4)/r^5] \\
Z_5^{+2} &= \sqrt{\frac{1155}{64\pi}}[(x^2 - y^2)(3z^3 - zr^2)/r^5] \\
Z_5^{+3} &= \sqrt{\frac{385}{512\pi}}[(x^3 - 3xy^2)(9z^2 - r^2)/r^5] \\
Z_5^{+4} &= \sqrt{\frac{3465}{256\pi}}[(x^4 - 6x^2y^2 + y^4)z/r^5] \\
Z_5^{+5} &= \sqrt{\frac{693}{512\pi}}[(x^5 - 10x^3y^2 + 5xy^4)/r^5] \\
\hline
Z_6^{-6} &= \frac{231}{64}\sqrt{\frac{26}{231\pi}}[(6x^5y - 20x^3y^3 + 6xy^5)/r^6] \\
Z_6^{-5} &= \sqrt{\frac{9009}{512\pi}}[(5x^4y - 10x^2y^3 + y^5)z/r^6]
\end{aligned}
$$

$$
\begin{aligned}
Z_6^{-4} &= \frac{21}{32}\sqrt{\frac{13}{7\pi}}[4(x^3y - xy^3)(11z^2 - r^2)/r^6] \\
Z_6^{-3} &= \frac{1}{32}\sqrt{\frac{2730}{\pi}}[(3x^2y - y^3)(11z^3 - 3zr^2)/r^6] \\
Z_6^{-2} &= \frac{1}{64}\sqrt{\frac{2730}{\pi}}[2xy(33z^4 - 18z^2r^2 + r^4)/r^6] \\
Z_6^{-1} &= \frac{1}{8}\sqrt{\frac{273}{4\pi}}[yz(33z^4 - 30z^2r^2 + 5r^4)/r^6] \\
Z_6^{0} &= \frac{1}{32}\sqrt{\frac{13}{\pi}}[(231z^6 - 315z^4r^2 + 105z^2r^4 - 5r^6)/r^6] \\
Z_6^{+1} &= \frac{1}{8}\sqrt{\frac{273}{4\pi}}[xz(33z^4 - 30z^2r^2 + 5r^4)/r^6] \\
Z_6^{+2} &= \frac{1}{64}\sqrt{\frac{2730}{\pi}}[(x^2 - y^2)(33z^4 - 18z^2r^2 + r^4)/r^6] \\
Z_6^{+3} &= \frac{1}{32}\sqrt{\frac{2730}{\pi}}[(x^3 - 3xy^2)(11z^3 - 3zr^2)/r^6] \\
Z_6^{+4} &= \frac{21}{32}\sqrt{\frac{13}{7\pi}}[(x^4 - 6x^2y^2 + y^4)(11z^2 - r^2)/r^6] \\
Z_6^{+5} &= \sqrt{\frac{9009}{512\pi}}[(x^5 - 10x^3y^2 + 5xy^4)z/r^6] \\
Z_6^{+6} &= \frac{231}{64}\sqrt{\frac{26}{231\pi}}[(x^6 - 15x^4y^2 + 15x^2y^4 - y^6)/r^6]
\end{aligned}
$$